

Title

Subtitle

by

Mikkel Metzsch Jensen

THESIS

for the degree of

MASTER OF SCIENCE



Faculty of Mathematics and Natural Sciences
University of Oslo

Spring 2023

Title

Subtitle

Mikkel Metzsch Jensen

© 2023 Mikkel Metzsch Jensen

Title

<http://www.duo.uio.no/>

Printed: Reprosentralen, University of Oslo

Abstract

Abstract.

Acknowledgments

Acknowledgments.

Contents

List of symbols?	ix
1 Introduction	1
1.1 Motivation	1
1.1.1 Friction	1
1.1.2 Thesis	1
1.2 Approach	2
1.3 Objective of the study	2
1.4 Contributions	2
1.5 Thesis structure	2
I Background Theory	3
2 Tribology - friction	7
2.1 Macroscale	7
2.1.1 Amontons' law	7
2.2 Microscopic scale	9
2.2.1 Surface roughness - Asperity theories	9
2.3 Nanoscale - Atomic scale	10
2.3.1 Frenkel-Kontorova	11
2.3.1.1 Commensurability	12
2.3.1.2 Kinetic friction	14
2.3.1.3 Temperature dependence	15
2.3.1.4 Smooth sliding	15
2.3.2 Experimental procedures	15
2.3.2.1 Scanning Probe Microscopy	15
2.3.2.2 Surface Force Apparatus (SFA)	16
2.3.3 (summary of) Expected frictional properties	16
2.3.3.1 Qualitatively	17
3 Molecular Dynamics	19
3.1 Potentials	19
3.1.1 General formulation of potentials (?)	19
3.1.2 Lennard Jones	19
3.1.3 Stillinger weber	20
3.1.4 Tersoff	21
3.2 Integration	22
3.2.1 Velocity Verlet	23
3.3 Thermostats	23
3.3.1 Langevin thermostat	24
3.3.2 Implementing Langevin	26
3.4 MD limitations (?)	26
3.5 LAMMPS	26

3.6 Fourier Transform (light)	26
4 Machine Learning (ML)	29
4.1 Feed forward network / Neural networks	29
4.2 CNN for image recognition	29
4.3 GAN (encoder + deoder)	29
4.4 Inverse desing using machine learning	29
4.5 Prediction explanation	29
4.5.1 Shapley	29
4.5.2 Lineariations	29
4.5.3 LRP	29
4.5.4 t-SNE	29
II Simulations	31
5 Defining the system	33
5.1 Region definitions (Sheet, pullblocks and substrate)	33
5.2 Numerical procedure	35
5.3 Creating the sheet	35
5.3.1 Graphene	35
5.3.2 Indexing	36
5.3.3 Removing atoms	37
5.4 Kirigami patterns	38
5.4.1 Pop-up	38
5.4.2 Honeycomb	38
5.4.3 Random walk	38
6 Pilot study	39
6.1 Friction simulation parameters	39
6.1.1 Pressure reference for normal load domain	41
6.2 Single friction simulation analysis	42
6.2.1 Force oscillations	42
6.2.2 Decompositions	43
6.2.3 Center of mass path	44
6.3 Defining metrics for dynamic and static friction	45
6.3.1 Dynamic friction	45
6.3.2 Static friction	46
6.4 Out of plane buckling	47
6.5 Investigating selected parameters	49
6.6 Normal force and stretch dependencies	51
6.6.1 Contact area	52
6.6.2 Stretch	52
6.6.3 Normal force	54
6.7 Computational cost	55
7 Generating data	57
8 Training forward network	59
9 Inverse design	61
10 Negative friction coefficient	63
10.1 Simulated coupling of normal force and stretch	63
10.2 Nanomachine coupling	63

Summary	65
10.3 Summary and conclusion	65
10.4 Outlook / Perspective	65
Appendices	67
Appendix A	69

List of symbols?

Maybe add list of symbols and where they are used like Trømborg.

Chapter 1

Introduction

1.1 Motivation

1.1.1 Friction

Friction is a fundamental force that takes part in almost all interactions with physical matter. Even though the everyday person might not be familiar with the term “friction” we would undoubtedly notice its disappearance. Without friction, it would not be possible to walk across a flat surface, lean against the wall or secure an object by the use of nails or screws [p. 5] [1]. Similarly, we expect a moving object to eventually come to a stop if not supplied with new energy, and we know intuitively that sliding down a snow covered hill is much more exciting than its grassy counterpart. It is probably safe to say that the concept of friction is well integrated in our everyday life to such an extent that most people take it for granted. However, the efforts to control friction dates back to the early civilization (3500 B.C.) with the use of the wheel and lubricants to reduce friction in translational motion [2].

Friction is a part of the wider field tribology derived from the Greek word *Tribos* meaning rubbing and includes the science of friction, wear and lubrication [2]. The most important motivation to study tribology is ultimately to gain full control of friction and wear for various technical applications. Especially, reducing friction is of great interest as this has tremendous advantages regarding energy efficiency. It has been reported that the monetary value of tribological problems has significant potential for economic and environmental improvements [3]:

“On global scale, these savings would amount to 1.4% of the GDP annually and 8.7% of the total energy consumption in the long term.” [4].

On the other side, the reduction of friction is not the only sensible application for tribological studies. Increasing friction might be of interest in the development of grasping robots or perhaps breaking system ([get some sourced examples maybe](#)), and ideally being able to turn friction up or down would be a groundbreaking step forward ([to much?](#)).

In the recent years an increasing amount of interest has gone into the understanding of the microscopic origin of friction, due to the increased possibilities in surface preparation and the development of nanoscale experimental methods such as the Friction Force Microscopy [5]. Nano-friction is also of great concern for the field of nano-machining where the frictional properties between the tool and the workpiece dictates machining characteristics [3].

[6]

1.1.2 Thesis

In recent papers by Hanakata et al. [7](2018), [6](2020) numerical investigations have showcased that the mechanical properties of a graphene sheet, yield stress and yield strain, can be altered through the introduction of so-called kirigami inspired cuts into the sheet. By the use of machine learning through accelerated search [7] and inverse design [6], they are able to extract cut pattern proposals which optimizes the mechanical properties in certain ways, e.g. stretchability or resistance to yield. This kind of study shows how numerical modelling and machine

learning can extremely usefull for the designing of metamaterials, i.e. materials with properties not found in naturally occurring materials. Hanakate et al. assert the complexity of the mehcanical properties of the kirigami cut sheet to the out of plane buckling accouring when the sheet is stretched.

Since it is generally accepted that the surface roughness is of great importance for frictional properties it can be hypothesized that the cut and stretch procedure can be exploited for the design of fricitonal metamaterials as well. If successfull, the link between stretch and friction properties might also rise to a metamaterial with tunable friction properties after the point of manufacturing. That is, a material which fricitonal properties will change during stretch and relaxtion. For such a material, coupling the normal load and stretch of the sheet through a nanomachine design would allow for an altered friction coefficient which in theory might take negative values in certain ranges of normal load. To the best of our knowledge kirigami has not yet been implemented to alter the frictional properties on a nanoscale. However, in a recent paper by Liefferink et al. [8](2021) it is reported that macroscale kirigami can be used to dynamically control the macroscale roughness of a surface by stretching which can be used to change the frictional coeffcient by more than one order of magnitude.

Something about machine learning and inverse design.

1.2 Approach

Explain my specific approach in more detail one this is settled in completely.

1.3 Objective of the study

1. Design a MD simulation to evaluate the frictional properties of the grapehene sheet under different variations of cut patterns, stretching and loading, among other physical variables.
2. Find suitable kirigami patterns which exhibit out of plane buckling under tensile load.
3. Create a procedure for generating variaiton of the selected kirigami patterns along with random walk based cut patterns in order to create a dataset for ML training.
4. Train a neural network to replace the MD simulation completely.
5. (Variation 1) Do an accelerated search using the ML network for exotic frictional properties such as low friction coefficients and a strong coupling between stretch and friction.
6. (Variation 2) Make a GAN network using the forward network in order to extract cut configuration proposals for above frictional properties.
7. Make a nanomachine or artifical numerical setup which couples normal load and stretch with the intention of making a proof of concept for negative friction coefficients.

1.4 Contributions

What did I actually achieve

1.5 Thesis structure

How is the thesis structured.

Part I

Background Theory

Small introtext to motivate this chapter. What am I going to go over here.

Chapter 2

Tribology - friction

Friction is a part of the wider field tribology which includes the study of friction, wear and lubrication between two surfaces in relative motion [1, p. 1]. In this thesis we will only concern ourselves with so-called wearless dry friction. That is, without any use of lubrication and without any resulting wear of the contacting surfaces. Tribological systems take place across a broad range of time and length scales, ranging from geological stratum layers involved in earthquakes [3] to microscopic atomistic processes, as in the gliding motion of a nanocluster of a nanomotor [9]. This vast difference in scale gives rises to different frictional mechanism being dominating at different scales. On a macro scale the system is usually subject to relatively high loads and speeds leading to high contact stresses and wear. On the other hand, the micro-/nanoscale regime occupies the opposite domain operating under relatively small loads and speeds with negligible wear [3] [2, p. 5]. While macroscale friction is often reduced into a few variables such as load, material type, speed and surface roughness it is clear that the micro-/nanoscale friction cannot be generalized under such a simple representation. On the micro-/nanoscale the tribological properties dominated by surface properties which will introduce an additional sensitivity variables such as temperature, humidity and even sliding history. The works of Bhushan and Kulkarni [10, (1996)] showed that the friction coefficient decreased with scale even though the materials used was unchanged. This reveals an intrinsic relationship between friction and scale as the contact condition is altered.

The phenomenological descriptions of macroscale friction cannot yet be derived from the fundamental atomic principles, and bridging the gap between different length scales in tribological systems remains an open challenge [9]. Hence, the following sections will be organized into macro-, micro- and nanoscale representing the theoretical understanding governing each scale regime. While our study of the graphene sheet is based on a nanoscale perspective the hypothesizing about application possibilities will eventually draw upon a macroscale perspective as well. Thus, we argue that a brief theoretical introduction to all three major scales is of high interest for a more complete interpretation of the findings in this thesis.

2.1 Macroscale

Our working definition of the *macroscale* is everything on the scale of visible everyday objects, which is usually denoted to the size of millimeters 10^{-3} m and above. Most importantly, we want to make a distinction to the *microscale*, where the prefix indicates the size of micrometers m^{-6} , and hence we essentially assign everything larger than *micro* to the term macroscale¹.

2.1.1 Amontons' law

In order to start and keep a solid block moving against a solid surface we must overcome certain frictional forces F_{fric} [1]. The static friction force F_s corresponds to the minimum tangential force required to initiate the sliding while the kinetic friction force F_k corresponds to the tangential force needed to sustain such sliding at steady speed. The work of Leonardo da Vinci (1452–1519), Guillaume Amontons (1663-705) and Charles de Coulomb (1736-1806) all contributed to the empirical law, commonly known as Amontons' law, which serves as a common base for macroscale friction. Amontons' law states that the frictional forces is entirely independent of contact

¹The width of a human hair is on the length scale 10^{-5} to 10^{-4} m which constitute a reasonable boundary between macro- and microscale which fit well with a lower bound of human perception capabilities.

area and sliding velocity. Instead, it relies only on the normal force F_N , acting perpendicular to the surface, and the material specific friction coefficient μ as

$$F_{\text{fric}} = \mu F_N. \quad (2.1)$$

Notice that the term *Normal force* is often used interchangeably with *load* and *normal load* although the latter terms refer to the applied force, pushing the object into the surface, while the first is the corresponding reaction force acting from the surface on the object. These forces are exactly equal in magnitude and hence we will not make a clear distinction in this thesis. On the same note, the frictional force is different from a conventional force which in the Newtonian definition acts on a body from the outside and make it accelerate [11]. Rather than being an independent external force the friction force is an internal *reaction* force opposing the externally applied “sliding” force.

The friction coefficient μ is typically different for the cases of static (μ_s) and kinetic (μ_k) friction, usually both with values lower than one and $\mu_s \geq \mu_k$ in all cases [1, p. 6]. The friction coefficient is taken to be a constant defined by either [11]

$$\mu = \frac{F_{\text{fric}}}{F_N}, \quad (2.2a) \quad \text{or} \quad \mu = \frac{dF_{\text{fric}}}{dF_N}. \quad (2.2b)$$

The first definition (2.2a) requires zero friction at zero load, i.e. $F_{\text{fric}} = 0$ at $F_N = 0$, while the second definition (2.2b) allows for a finite friction force at zero load since the coefficient is instead given by the slope of the F_{fric} versus F_N curve. However, in reality the friction coefficient is not truly a material specific constant as it is often found to vary under different conditions such as humidity or smooth and rough morphologies of the sliding surfaces [11].

Although Amontons' law has been successful in its description of the majority of rubbing surfaces, involving both dry and lubricated, ductile and brittle and rough and smooth (as long as they are not adhesive) surfaces [11], it has its limitations. It is now known that eq. (2.1) is not valid over a large range of loads and sliding velocities and that it completely breaks down for atomically smooth surfaces in strongly adhesive contact [11]. The independency of sliding velocity disappears at low velocities as thermal effects becomes important and for high velocities due to inertial effects [1, pp. 5-6]. For the case of static friction, it was later discovered to be dependent on the so-called contact history with increasing friction as the logarithm of time of stationary contact.

In cases where amontons' law breaks down we might still use the conceptual definition of the friction coefficient as defined by (2.2b). Especially, in the context of achieving negative friction coefficients (in certain load ranges) we would refer to this definition, since (2.2a) would imply a truly unphysical situation of the frictional force acting in the same direction as the sliding motion which would accelerate the object indefinitely².

Due to the empirical foundation of Amontons' law it does not provide any physical insight into the underlying mechanisms of friction. However, as we will later discuss in more detail, we can understand the overall phenomena of friction through statistical mechanics by the concept of *equipartition of energy* [9]. A system in equilibrium has its kinetic energy uniformly distributed among all its degrees of freedom. When a macroscale object is sliding in a given direction it is clearly not in equilibrium since one of its degrees of freedom carries considerable more kinetic energy. Thus, the system will have a tendency to transfer that kinetic energy to the remaining degrees of freedom as heat. This heat will dissipate to the surroundings and the object will slow down as a result. Hence, we can understand friction simply the tendency of going toward equilibrium energy equipartitioning among many interacting degrees of freedom [9]. From this point of view it is clear that friction is an inevitable part of contact physics, but even though friction cannot be removed altogether, we are still capable of manipulating it in useful ways.

The attentive reader might point out that we have already moved the discussion partly into the microscopic regime as *statistical mechanics* generally aim to explain macroscale behaviour by microscopic interactions. In fact, this highlights the necessity to consider smaller scales in order to achieve a more fundamental understanding of friction.

²You would most likely have a good shot at the Nobel Prize with that paper.

2.2 Microscopic scale

Going from a macro- to microscale perspective, a length scale of order 10^{-6} m, it was realized that most surfaces is in fact rough [12]. The contact between two surfaces consist of numerous smaller contact point, so-called asperities, for which the friction between two opposing surfaces involves interlocking of those asperities as visualized in figure 2.1. Small junctions of asperities are formed due to contact pressure and adhesion [3]

In the macroscale perspective of Amonton's law we refer to time- and space-averaged values, i.e. the "apparent" contact area and the average sliding speed [11]. However, microscopically we find the real contact area to be smaller than the macroscale apparent area and the shearing of local microjunctions can happen at large fluctuations or in a stick-slip fashion.

It is generally accepted that friction is caused by two mechanism: mechanical friction and chemical friction [3]. The mechanical friction is the "plowing" of the surface by hard particles or said asperities with an energy loss attributed to deformations of the asperity. While plastic deformations, corresponding to wear, gives rise to an obvious attribution for the energy loss, elastic deformations is also sufficient in explaining energy loss due to phonon excitations. In fact the assumption of plastic deformations has been critizised as this is theorized only to be present in the beginning of surface contact [13]. When machine parts slide against each other for millions of cycle the plastic deformation would only take place in the beginning until the system reaches a steady state with only elastic deformation taking place. The chemical friction arrises from adhesion between microscopic contacting surfaces, with an energy loss attributed to breaking and forming of bonds.

2.2.1 Surface roughness - Asperity theories

Asperity theories are based on the observation that microscopic rough surfaces, with contacting asperities each with a contact area of A_{asp} , will have a true contact area $\sum A_{\text{asp}}$ much smaller than the apparent macroscopic area [3]. The friction force has been shown to be proportional to the true contact area as

$$F_{\text{fric}} = \tau \sum A_{\text{asp}},$$

where τ is an effective shear strength of the contacting bodies. Note that this is compatible with Amontons' law in eq. (2.1) by having a linear relationship between the real contact area and the applied load. In figure 2.1 we see a visualization on how the contact area might intuitively increase with load as the asperity tips is deformed (plastically or elastically) into broader contact points.

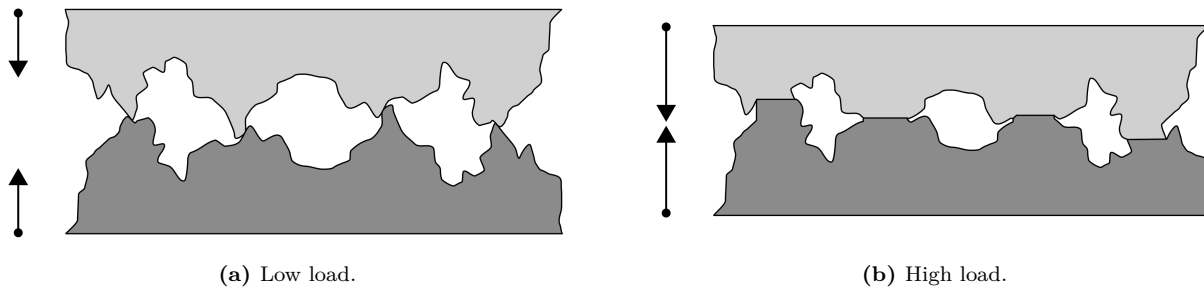


Figure 2.1: Qualitative illustration of the microscopic asperity deformation under increasing load from frame (a) to (b) [14]. While this figure evidently portrays plastic deformation the concept of increased contact area under increased load applies for elastic deformation as well.

Many studies have focused on single asperity contacts to reveal the relationship between the contact area and F_N (13-15 from [12]). By assuming perfectly smooth asperities, with radii of curvature from micrometers all the way down to nanometers, continuum mechanics can be used to predict the deformation of asperities as load is applied. A model for non-adhesive contact between homogenous, isotropic, linear elastic spheres was first developed by Hertz (17 from [12]), which predicted $A_{\text{asp}} \propto F_N^{2/3}$. Later adhesion effects were included in a number of subsequent models, including Maugis-Dugdale theory (18 from [12]), which also predicts a sublinear relationship between A_{asp} and F_N . Thus, the common feature of all single-asperity theories is that A_{asp} is a

sublinear function of F_N , leading to a similar sublinear relationship for $F_{\text{fric}}(F_N)$, which fails to align with the macroscale observations modelled by Amontons' law (eq. (2.1)).

Concurrently with single-asperity studies, roughness contact theories are being developed [12, 8-10, 16 in] to bridge the gap between single asperities and macroscopic contacts [12]. A variety of multi-asperity theories has attempted to combine single asperity mechanics by statistical modelling of the asperity height and spatial distributions [13]. This has led to a partially success in the establishment of a linear relationship between A_{asp} and F_N . Unfortunately, these results are restricted in terms of the magnitude of the load and contact area, where multi-asperity contact models based on the original ideas of Greenwood and Williamson [15] only predicts linearity at vanishing low loads, or Persson [16] which works for more reasonable loads but only up to 10-15 % of the macroscale contact area. However, as the load is further increased all multi-asperity models predict the contact area to fall into the sublinear dependency of normal force as seen for single aperity theories as well [13].

2.3 Nanoscale - Atomic scale

Going from a micro- to a nanoscale, on the order of 10^{-9} m, it has been predicted that continuum mechanics will break down [17] due to the discreteness of individual atoms. Note that atom spacing lies in the domain of a few ångströms Å (10^{-10} m) and thus we take the so-called atomic-scale to be a part of the nanoscale regime. In a numerical study by Mo et al. [12] (considering asperity radii of 5-30 nm) it has been shown that the asperity area A_{asp} , defined by the circumference of the contact zone, is sublinear with F_N . This is accommodated by the observation that not all atoms within the circumference make chemical contact with the substrate. By modelling the real contact area $A_{\text{real}} = N A_{\text{atom}}$, where N is the amount of atoms within the range of chemical interaction and A_{atom} the associated surface area for an atom, they found a consistent linear relationship between friction and the real contact area. Without adhesive forces this lead to a similar linear relationship $F_{\text{fric}} \propto F_N$, while adding van der Waals adhesion to the simulation gave a sublinear relationship, even though the $F_{\text{fric}} \propto A_{\text{real}}$ was maintained. This result emphasizes that the contact area is still expected to be play an important role at the nanoscale for asperity theory. It is simply the definition of the contact area that undergoes a change when transitioning from micro- to nanoscale.

However, considering the simulation setup of our numerical study, a flat sheet on a flat substrate, the lack of asperities make it unfounded to rely on asperity theories. Although both numerical and experimental research have been done for so-called nanoflakes sliding on a substrate, no investigation is reported on the dependence of friction force on contact area (to the best of my knowledge at least). One reasonable explanation is that the contact area is already maxed out for atomic smooth surfaces. Since a dependency on normal load is still reported in most nanoflake studies (see section 2.3.3 or give details on studies here?), this suggests that some other mechanisms are governing friction at this level. Before diving into alternative theoretical approaches to address this issue we point out that exactly this transition, between nanoscale asperities and atomic smooth surfaces, is of outermost importance for the objective of the thesis. By introducing kirigami cuts and stretching the sheet we expect to see an out of plane buckling which induce an ensemble of asperities on the sheet. Hence, we might hypothesize that such a transition will contribute to a significant change in the governing mechanism of friction bridging two (poorly understood) theoretical domains

In the lack of noteworthy structural asperities, friction can instead be modelled as a consequence of the rough potential of the atomic landscape. A series of models builds on this idea by considering different ways for the atoms to interact interatomically, with the moving body, and the substrate. In figure 2.2 three of the most common 1D models is displayed. The time-honored Prandtl-Tomlinson (PT) model describes a point-like tip sliding over a space-periodic fixed crystalline surface with a harmonic coupling to the *moving body*. This is analog to that of an experimental cantilever used for Atomic Force Microscopy (see section 2.3.2.1). Further extensions was added in the Frenkel-Kontorova (FK) model by substituting the tip with a chain of harmonic coupled atoms dragged from the end (I am not sure that the figure is 100% correct by drawing a spring like that), and finally combined in the Frenkel-Kontorova-Tomlinson (FKT) with the addition of a harmonic coupling between the chain and the moving body. In the following we will discuss the FK model as this gives provides a sufficient foundation for the understanding of smooth nanoscale friction.

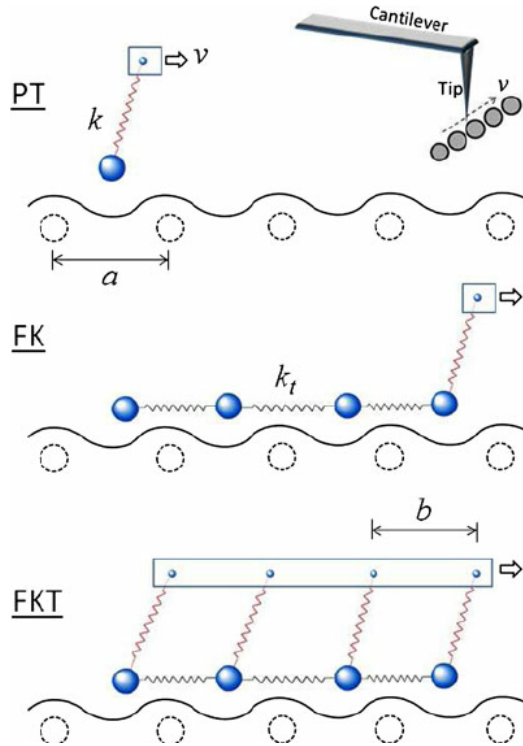


Figure 2.2: Temporary figure from https://www.researchgate.net/figure/illustrations-of-the-1D-PT-FK-and-FKT-models-Largefig1_257670317

2.3.1 Frenkel-Kontorova

The standard Frenkel-Kontorova (FK) model consists of a 1D chain of N classical particles of equal mass, representing atoms, interacting via hamornic forces and moving in a sinusoidal potential as sketched in figure 2.3 [9]. The hamiltonian is

$$H = \sum_{i=1}^N \left[\frac{p_i^2}{2m} + \frac{1}{2}K(x_{i+1} - x_i - a_c)^2 + \frac{1}{2}U_0 \cos\left(\frac{2\pi x_i}{a_b}\right) \right], \quad (2.3)$$

where the atoms are labelled sequently $i = 1, \dots, N$. The first term $p_i^2/2m$ represents the kinetic energy with momentum p_i and mass m . Often the effetc of inertia are neglected, reffered to as the static FK model, while the inclusion, as shown here in eq. (2.3), is known as the dynamic FK model [5]. The next term describes the harmonic interaction with elastic constant K , nearest neighbour distance $\Delta x = x_{i+1} - x_i$ and corresponding nearest neighbour equilibrium distance a_c . The final term represents the periodic substrate potential (external potential on site) with amplitude U_0 and period a_b . Different boundary choices can be made where both free ends and periodic conditions gives similar results. The choice of fixed ends however makes the chain incapable of sliding.

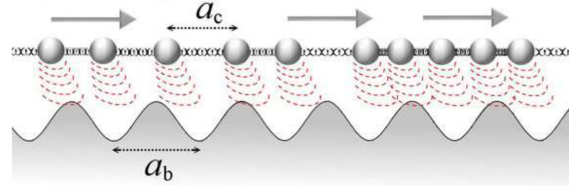


Figure 1. A sketch of the FK model, showing the two competing lengths: the average interparticle spacing and the lattice periodicity of the substrate.

Figure 2.3: [Temporary figure from [9]]

To probe static friction one can apply an external adiabatically increasing force until sliding accours. This corresponds to the static FK model, and it turns out that the sliding properties are entirely governed by its topological excitations referred to as so-called *kinks* and *antikinks*

2.3.1.1 Commensurability

We can subdivide the frictional behaviour in terms of commensurability, that is, how well the spacing of the atoms match the periodic substrate potential. We describe this by the length ratio $\theta = a_b/a_c = N/M$ where M denotes the number of minemas in the potential (within the length of the chain). A rational number for θ means that we can align the atoms in the chain perfectly with the minemas, without stretching the chain, corresponding to a *commensurate* case. If θ is irrational the chain and substrate cannot fully align without stretching of the chain, and we denote this as being *incommensurate*.

We begin with the simplest commensurate case of $\theta = 1$ where the spacing of the atoms matches perfectly with the substrate potential periodicity, i.e. $a_c = a_b$, $N = M$. The ground state (GS) is the configuration where each atom fits in one of the substrate minemas. By adding an extra atom we would effectively shift over some atoms, away from this ideal state, giving rise to a kink excitation, i.e. two atoms will have to “share” the same potential corrugation as sketched in figure 2.5. On the other hand, removing an atom from the chain results in an antikink excitation where one potential corrugation will be left “atomless”. In order to reach a local minimum the kink (antikink) will expand in space over a finite length such that the chain undertakes a local compression (expansion). When applying a tangential force to the chain it is much easier for an excitation to move along the chain than it is for the non-excited atoms since the activation energy ϵ_{PN} for a kink/antikink displacement is systematically smaller (often much smaller) than the potential barrier U_0 . Thus, the motion of kinks (antikinks), i.e. the displacement of extra atoms (atom vacancies), is represententing the fundamental mechanism for mass transport. These displacements are responsible for the mobility, diffusivity and conductivity within this model.

In the ideal zero temperature commensurable case with an adiabatical increase in force, all atoms would be put into an accelerating motion as soon as the potential barrier energy is present ($\sim NU_0$ for sufficiently stiff springs). However, in reality any thermal excitation would excite the system before this point is reached resulting in kink-antikink pairs traveling down the chain. For a chain of finite length these often accrue at the end of the chain running in opposite direction. As a kink travels down the chain the atoms is advanced by one lattice spacing a_b along the substrate potential. This cascade of kink-antikink exications is shown in figure 2.4

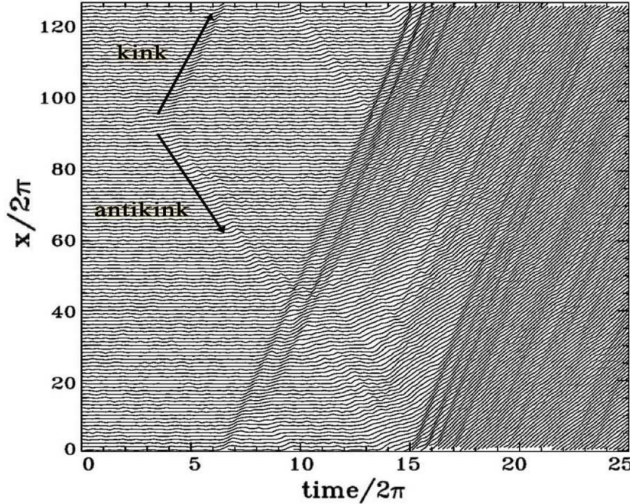


Figure 2. Time dependence of the atomic trajectories for the fully matched ($\theta = 1$) FK model at the (low-temperature) onset of depinning. Motion starts with the nucleation of a kink-antikink pair. The kink and the antikink depart in opposite directions cross the periodic boundary conditions, and collide quasielastically. A second kink-antikink pair forms in the wake of the initial kink. Further kink-antikink pairs are generated, with an avalanche-like increase of the kink-antikink concentration, eventually leading to a sliding state. Adapted from Ref. [21], Copyright (1997) by The American Physical Society.

Figure 2.4: **Temporary** figure from [9]

For the 2D case where an island (or flake) is deposited on a surface, in our case the graphene sheet on the Si substrate, we generally also expect the sliding to be initiated by kink-antikink pairs at the boundary.

For the case of incommensurability, i.e. $\theta = a_b/a_c$ is irrational, the GS is characterized by a sort of ‘‘staircase’’ deformation. That is, the chain will exhibit regular periods of regions where the chain is slightly compressed (expanded) to match the substrate potential, separated by kinks (antikinks), where the increased stress is eventually released through a localized expansion (compression) as illustrated in figure 2.5 Go through this last part again. Even though this is what the source says I’m not quite sure I understand why it is not opposite ‘‘...released through a localized compression (expansion)’’?



Figure 2.5: **Temporary** figure from [urlhttp://www.iop.kiev.ua/~obraun/myreprints/surveyfk.pdf](http://www.iop.kiev.ua/~obraun/myreprints/surveyfk.pdf) p. 14. Incommensurable case ($\theta = ?$) where atoms sit slightly closer than otherwise dictated by the substrate potential for which this regularly result in a kink here seen as the presence of two atoms closely together in one of the potential corrugations.

The incommensurable FK model contains a critical elastic constant K_c , such that for $K > K_c$ the static friction F_s drops to zero, making the chain able to initiate a slide at no energy cost, while the low-velocity kinetic friction is dramatically reduced. This can be explained by the fact that the displacement occurring in the incommensurable case will yield just as many atoms climbing up a corrugation as there are atoms climbing down. For a big (infinite) chain this will exactly balance the forces making it non-resistant to sliding. Generally, incommensurability guarantees that the total energy (at $T = 0$) is independent of the relative position to the potential. However, when sliding freely a single atom will eventually occupy a maximum of the potential. When increasing the potential magnitude U_0 or softening the chain stiffness, lowering K , the possibility to occupy such

a maximum disappears. This marks the so-called Aubry transition at the critical elastic constant $K = K_c(U_0, \theta)$ where the chain goes from a free sliding to a *pinned state* with a nonzero static friction. K_c is a discontinuous function of the ratio θ , due to the reliance on irrational numbers for incommensurability. The minimal value $K_c \simeq 1.0291926$ in units $[2U_0(\pi/a_b)^2]$ is achieved for the golden-mean ratio $\theta = (1 + \sqrt{5}/2)$. Notice that the pinning is provided despite translational invariance due to the inaccessibility to move past the energy barrier which act as a dynamical constraint. The Aubry transition can be investigated as a first-order phase transition for which power laws can be defined for the order parameter. This is beyond the scope of this thesis as we merely are going to point to the FK model for the understanding of stick-slip behaviour and the concept of commensurability.

The phenomena of non-pinned configurations is named *superlubricity* in tribological context. Despite the misleading name this refers to the case where the static friction is zero while the kinetic friction is nonzero but reduced. For the case of a 2D sheet it is possible to alter the commensurability by changing the orientation of the sheet relative to the substrate. This has been shown for a graphene flake sliding over a graphite surface (multiple layers of graphene) [18] as shown in figure 2.6. We clearly see that friction changes as a function of orientation angles with only two spikes of considerable friction force.

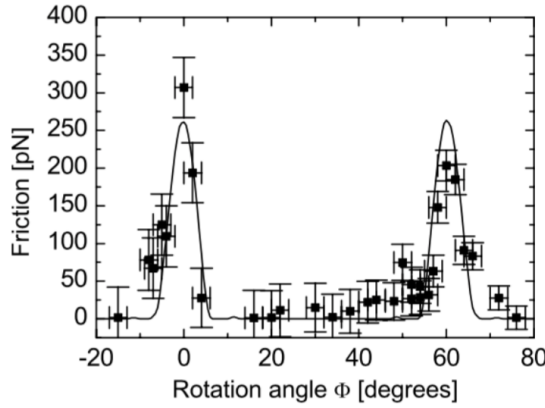


Fig. 6. Average friction force versus rotation angle Φ of the graphite sample around an axis normal to the sample surface. Two narrow peaks of high friction are observed at 0° and 61° , respectively. Between these peaks a wide angular range with ultra-low friction, close the detection limit of the instrument, is found. The first peak has a maximum friction force of 306 ± 40 pN, and the second peak has a maximum of 203 ± 20 pN. The curve through the data points shows results from a Tomlinson model for a symmetric 96-atom graphite flake sliding over the graphite surface (for details about the calculation see [39]).

Figure 2.6: **Temporary** figure from [18] showing superlubricity for incommensurable orientations between graphene and graphite. **temporary**

2.3.1.2 Kinetic friction

In the FK model the kinetic friction is primarily caused by resonance between the sliding induced vibrations and phonon modes in the chain [5]. The specific dynamics is found to be highly model and dimension specific, and even for the 1D case this is rather complex. However, we make a simplified analysis of the 1D case to showcase the reasoning behind the phenomena.

When all atoms are sliding rigidly with center of mass velocity v_{CM} the atoms will pass the potential maxima with the so-called *washboard frequency* $\Omega = 2\pi v_{CM}/a_b$. For a weak coupling between the chain and the potential we can use the zero potential case as an approximation for which the known dispersion relation for the

1D harmonic chain is given [Kittel (add to bibliography)]

$$\omega_k = \sqrt{\frac{4K}{m}} \left| \sin\left(\frac{k}{2}\right) \right|,$$

where ω_k is the phonon frequency and $k = 2\pi i/N$ the wavenumber with $i \in [N/2, N/2)$. Resonance will occur when the washboard frequency Ω is close to the frequency of the phonon modes ω_q in the chain with wavenumber $q = 2\pi a_c/a_b = 2\pi\theta^{-1}$ or its harmonics nq for $n = 1, 2, 3, \dots$ [19]. Thus, we can approximate the resonance COM speed as

$$\begin{aligned} n\Omega &\sim \omega_{nq} \\ n\frac{2\pi v_{CM}}{a_b} &\sim \sqrt{\frac{4K}{m}} \left| \sin\left(\frac{2n\pi\theta^{-1}}{2}\right) \right| \\ v_{CM} &\sim \frac{\sin(n\pi\theta^{-1})}{n\pi} \sqrt{\frac{Ka_b^2}{m}}. \end{aligned}$$

When the chain slides with a velocity around resonance speed, the washboard frequency can excite acoustic phonons which will dissipate to other phonon modes as well. At zero temperature the energy will transform back and forth between internal degrees of freedom and center of mass movement of the chain. Hence, at zero temperature this is in fact theorized to speed up the translational decay. However, for the more realistic case of a non-zero temperature the substrate serves as a thermostat, for which energy will dissipate from the chain to the substrate degrees of freedom, giving rise to kinetic friction. This suggests that certain sliding speeds will exhibit relatively big kinetic friction while others will be subject to extremely low kinetic friction. Simulations of concentric nanotubes in relative motion (telescopic sliding) have revealed the occurrence of certain velocities at which the friction is enhanced, corresponding to the washboard frequency of the system [9]. The friction response was observed to be highly non-linear as the resonance velocities were approached.

A common way to model the non-zero temperature case is by the use of a Langevin thermostat, which models the dissipation of heat by adding a viscous damping force and thermal fluctuations by the addition of Gaussian random forces with variance proportional to the temperature (This is covered in more details in section 3.3.1). In combination, this gives rise to a kinetic friction that is both velocity and temperature dependent.

By extending the FK model into 2D [5] it can be shown numerically that the friction coefficient generally increases with increasing velocity and temperature respectively, although the specific of the trend is highly sensitive to model parameters.

2.3.1.3 Temperature dependence

Might find something interesting here [20] or [21].

2.3.1.4 Smooth sliding

Find a suitable place to introduce smooth sliding. Above certain velocities the stick-slip motion disappears. [1, p. 142-ish]

2.3.2 Experimental procedures

Experimentally, the study of nanoscale friction is challenging due to the low forces on the scale of nano-newtons along with difficulties of mapping nanoscale topography [1, p. ?]. Numerically, simulations provide full transparency regarding atomic-scale structures and sampling of forces, velocities and temperature. Of course, this comes with a possible cost of realism as we will address later (do we actually). In order to compare numerical and experimental results, the experimental procedures are often mirrored in simulations. Thus, it is relevant to address the most common experimental techniques before designing a simulation.

2.3.2.1 Scanning Probe Microscopy

Scanning probe microscopy (SPM) includes a variety of experimental methods which is used to examine surfaces with atomic resolution [22, p. 6-?]. This was originally developed for surface topography imaging, but today

it plays a crucial role in nanoscale science as it is used for probe-sampling regarding tribological, electronic, magnetic, biological and chemical character. The family of methods involving the measurement of forces is generally referred to as *scanning force microscopies* (SFM) or for friction purposes *friction force microscopes* (FFM).

One such method arose from the *atomic force microscope*, which consist of a sharp micro-fabricated tip attached to a cantilever force sensor, usually with a sensitivity below 1 nN. The force is measured by recording the bending of the cantilever, either as a change in electrical conduction or more commonly, by a light beam reflected from the back of the cantilever into a photodetector [1]. By adjusting the tip-sample height to keep a constant normal force while scanning across the surface this can be used to produce a surface topography map. By tapping the material (dynamic force microscopy) with sinusoidally vibrated tip the effects from friction and other disturbing forces can be minimized in order to produce an even clearer image ([include example, preferable showing the surface structure of graphene](#)). However, when scanning perpendicularly to the cantilever axis, one is also able to measure the frictional force as torsion of the cantilever. By having four quadrants in the photodetector (as shown in figure 2.7), one can simultaneously measure the normal force and friction force as the probes scans accross the surface.

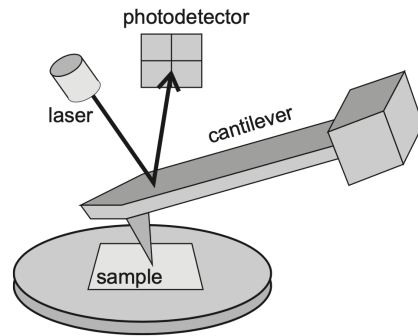


Figure 17.1 Schematic diagram of a beam-deflection atomic force microscope.

Figure 2.7: [Temporary](#) figure from [1, p. 184]

AFM can also be used to drag a nanoflake accross the substrate as done by Dienwiebel et al. [18], where a graphene flake was attached to a FFM tip and dragged accross graphite. However, this makes the normal loading concentrated to a single point on the flake.

2.3.2.2 Surface Force Apparatus (SFA)

I think this refers to having two interfaces sliding against each other with (optionally I think) lubrication between. This is often mirrored in MD simulations and often experimental results refer to this. So it might be worth saying a few words about, but I'm not sure yet.

2.3.3 (summary of) Expected frictional properties

The structural setup of our simulation is most reminiscent a graphene flake sliding on a substrate. This has been studied numerically in molecular dynamic simulations by Zhu and Li [23, 2018] for a graphene flake on a gold substrate and by Zhang et al. [24](2019) on a diamond substrate, and in a tight-binding simulation by Bonelli et al. [25](2009) for graphene on graphite. Experimental studies of a graphene flake attached to an AFM is done by Dienwiebel et al. [18, 2005] and Feng et al. [26, 2013] sliding on graphite, but these are mainly concerned with superlubricity due to flake orientation commensurability.

In our study we simulate a graphene flake on a silicon substrate which deviates slightly from the above-mentioned references by having a different material combination. Additionally, the normal force is only applied to the ends of the sheet which might have an important effect. Obviously stretching and cutting the sheet will separate our study dramatically from the references, but we aim to compare the frictional properties to the references before applying stretch or cuts.

In the following we summarize the qualitative expectations for the nanofriction behaviour for the unstretched and non-cut graphene sheet.

2.3.3.1 Qualitatively

1. **Stick slip:** Generally we expect to observe periodic stick-slip motion with a period matching the lattice constant(s) involved [12]. This was both present in the MD simulations [23], [24] and in the experiment by [18]. In AFM and SFA experiments, the stick-slip motion tends to transition into smooth sliding when the speed exceeds $\sim 1 \mu\text{m/s}$ while in MD modelling the same transition is observed in the $\sim 1 \text{ m/s}$ region [9]. Since we use a sliding speed of 20 m/s we might transition into smooth sliding. This 6 order of magnitude discrepancy has been largely discussed in connection to simplifying assumptions in MD simulations. Bonelli et al. [25] found that the stick-slip behaviour was present when the cantilever-tip-flake coupling was done with a relatively soft springs in contrast to hard springs which inhibited it.
2. **Static friction:** As highlighted in the FK model static friction will be sensitive to commensurability, which will additionally be affected by flake size. Reguzzoni and Righi [27] have shown that the effective commensurability will increase drastically below a critical flake radius on the order of 10 Å. Macroscopically we expect to see a logarithmic increase in static friction with contact time before sliding [28], and hence due to the short time-span of the static contact before dragging, it is not obvious to determine whether a significant static friction peak will be found. Also, the static friction best asserted by increasing the tangential sliding force slowly which is not the case in our simulation, especially considering that we are going to move the sheet rigidly (infinite spring constant) without any slack of a soft spring. Edge related origin of the pinning effects suggest that static friction can increase with sheet size up to a factor $A \propto A^{1/2}$, but this is also reported to be specific of the contact shape [9].
3. **Orientation (friction anisotropy):** As predicted by the FK model and confirmed both numerically [23], [24] and experimentally [18], [26] we expect a dependence of friction force on orientation due to changing commensurability. Zhu and Li [23] (gold substrate) reported the highest friction when sliding along the armchair direction, while Zhang et al. [24] (diamond substrate) found the zigzag-direction to give the highest friction force (also the most evident stick-slip behaviour in this direction).

By consulting with the most related numerical and experimental studies, while also considering the theoretical gap between smooth atomic contact and asperity theory, we have summarized an evaluation of the most important quantitative trends expected from our numerical results in table ??.

Table 2.1: Quantitative nano friction dependence on various variables. work in progress.

Variable	Dependency	Numerical studies	Experimental
Normal force F_N	$F_{\text{fric}} \propto F_N^\alpha$ $\alpha \leq 1$	Zhang et al. [24] finds a seemingly linear relationship $F_{\text{fric}} \propto F_N$ while Bonelli et al. [25] reports a sublinear relationship. The latter corresponds with that of nanosasperity simulations where Mo et al. [12], using an amorphous carbon tip on a diamond sample, also found a sublinear relationship when including adhesion and linear without adhesion.	Experimentally rather different trends have been observed, although the majority agree on increasing friction with increasing load [1, p. 200]. For the graphebne flake Dienwiebel et al. [18] found a seemingly non-dependent relationship while Feng et al. [26] did not report on this. FFM analog to the single asperity setup have yielded both linear relationship [11] (silicon tip on gold) while Schwarz et al. [29] found that FFM with well-defined spherical tips matched with theoretical results (DMT, elastic spheres pressed together [1, p. 200]), yielding a power law $F_{\text{fric}} = F_N^{2/3}$.
Velocity v	$F_{\text{fric}} \propto \ln v$ (exp.) or $F_{\text{fric}} \propto v$ (num.)	Studies of gold clusters on graphite suggest that friction is viscous, i.e. proportional to velocity [9].	Logaritmic velocity dependence of friction has been measured for nanotip friction [1, p. 201] associated to thermal activation and possibly the time available to form bond between the tip and the substrate. At higher velocities thermally activated processes are less important and friction becomes independent of velocity. This has been observed for Si tips and diamond, graphite and amorphous carbon surfaces with scan velocities above $1 \mu/\text{s}$.
Temperature T	Either increase (MD) or decrease as $F_{\text{fric}} \propto \exp(1/T)$ (experimental)	Zhang et al. [24] found simply that friction increased with temperature. The [9] gold cluster on graphite study (get reference) found that the temperature dependence was dependend on velocity regime. Low speed (diffusive) friction decreases upon heating while high speed (ballistic) friction rises with temperature.	Zhao et al. [20] found $F_{\text{fric}} \propto \exp(1/T)$.
Real contact area A	$F_{\text{fric}} \propto A$	Mo et al. [12] found that $F_{\text{fric}} \propto A$ where A is the real contact area defined by atoms within chemical range. This is not studied for the case of a nanoflake where the contact area is presumably rather constant.	

Chapter 3

Molecular Dynamics

Thanks to advances in computing algorithms and hardware the recent years has witnessed a remarkable increase in our ability to simulate tribological processes in realistic nano-frictional system [9]. A Molecular dynamics (MD) simulation can be considered as computational “experiment”. Given a set of initial conditions and a mathematically model for interatomic forces we can solve Newton’s (or equivalent) equation of motion by numerical integration [p. 303]BHUSHAN20051507. The interatomic forces are derived from interparticle interaction potentials, which is the heart of MD simulations and the specific choice of potentials can often be quite challenging.

Alternatives to the MD simulation like Ab initio methods calculate the interaction based on quantum mechanics (solving schrödinger) right?

3.1 Potentials

The potentials used in our MD simulation is mainly based on the of Li et al. [30] which have a somewhat similar MD friction simulation setup. Li et al. impose a Silicon tip on the graphene sheet supported by a Silicon substrate where we slide the whole sheet upon the substrate. Nonetheless, this serves as a good anchor for the methodology of the setup. The covalent bonds of C-C in graphene and Si-Si in the substrate is described by the Tersoff and Stillinger–Weber potentials, respectively. A typical 12-6 Lennard–Jones potential is used to describe the van der Waals adhesive interaction between graphene and the substrate.

3.1.1 General formulation of potentials (?)

On a general note we can generalize the n-body potential as the expansion in orders of participating atoms as

$$E = \sum_i V_1(\mathbf{r}_i) + \sum_{\substack{i,j \\ i < j}} V_2(\mathbf{r}_i, \mathbf{r}_j) + \sum_{\substack{i,j,k \\ i < j < k}} V_3(\mathbf{r}_i, \mathbf{r}_j, \mathbf{r}_k) + \dots,$$

where \mathbf{r}_n is the position of the n th particle and V_m is called an m -body potential [31]. The first one-body term corresponds to an external potential, followed by the two-body term, the three-body term and so on. The simplest model that includes particle interaction is the pair potential truncating the expansion after the two-body term. A general feature of the pair potentials is that they favor close-packed structures which is unsuited to describe covalent bonds that take more open structures. In particular, pair potentials are completely inapplicable to strongly covalent systems [31]. In order to accomodate the description of covalent bonds the natural step is thus to include the next step of the expansion, the three-body terms, as we will see for the modeling of the C-C bonds in the graphene sheet and the Si-Si bonds in Silicon substrate. For the interaction between the sheet and the substrate we use a Lennard Jones pair potential describing the non-bonded van der Waals interaction. This simple interaction model between the moving object and substrate has come to be the standard in friction simulations [23], [32], [33], [3].

3.1.2 Lennard Jones

TODO: Add potential curve figure

This sections is based on [34], [35], [36].

The Lennard-Jones (LJ) model is probably one of the most famous pair potentials used in MD simulations. LJ models the potential energy between two non-bonding atoms solely based on interatomic distance. The model accounts for attractive forces arising from dipole-dipole, dipole-induced dipole and London interactions, and repulsive forces that capture the hard core of overlapping wave functions at small distances (**double check this statement**). Thus, it assumes neutrally charged atoms and was originally proposed for noble gases. The classical 12-6 version of the model (referring to the power law of the repulsive and attractive forces respectively) reads

$$E = 4\epsilon \left[\left(\frac{\sigma}{r} \right)^{12} - \left(\frac{\sigma}{r} \right)^6 \right], \quad r < r_c, \quad (3.1)$$

where r is the interatomic distance with cut-off r_c , ϵ is the depth of the potential well and σ the interatomic distance where the potential is zero. By solving for the potential minimum ($dE/dr = 0$) we find the equilibrium distance to be $r_0 = \sigma 2^{1/6}$. This makes for a slightly more intuitive interpretation of σ which effectively sets the equilibrium distance between atoms, i.e. the dividing line for which the force is repulsive or attractive.

3.1.3 Stillinger weber

TODO: Add potential figure and/or figure illustrating three body angles.

This section is based on [[37], [38]]

The stillinger weber potential takes the form of a three body potential

$$E = \sum_i \sum_{j>i} \phi_2(r_{ij}) + \sum_i \sum_{j\neq i} \sum_{k>j} \phi_3(r_{ij}, r_{ik}, \theta_{ijk}),$$

where r_{ij} denotes the distance between atom i and j and θ_{ijk} the angle between bond ij and jk . The summations is over all neighbours j and k of atom i within a cut-off distance $r = a\sigma$.

The two-body term ϕ_2 builds from the LJ model with the addition of an exponential cutoff term

$$\phi_2(r_{ij}) = A_{ij}\epsilon_{ij} \left[B_{ij} \left(\frac{\sigma_{ij}}{r_{ij}} \right)^{p_{ij}} - \left(\frac{\sigma_{ij}}{r_{ij}} \right)^{q_{ij}} \right] \exp\left(\frac{\sigma_{ij}}{r_{ij} - a_{ij}\sigma_{ij}}\right). \quad (3.2)$$

The model parameters A , ϵ , B , σ , p , q and a comes with i, j indices to indicate that these parameters should be specified for each unique pair of atom types. However, in our case we will only provide a single value for each model parameter as we are exclusively dealing with Si-Si bonds. We see that the first term in eq. (3.2) is reminiscent of the LJ model in eq. (3.1) while the last term effectively drives the potential to zero at $r = a\sigma$, which is thus the chosen cut-off distance for the potential evaluation. With the model parameters for the Si-Si modelling (see table 3.1) the cut-off becomes ~ 3.8 Å.

The three body term includes an angle dependency as

$$\phi_3(r_{ij}, r_{ik}, \theta_{ijk}) = \lambda_{ijk} \epsilon_{ijk} \left[\cos \theta_{ijk} - \cos \theta_{0,ijk} \right]^2 \exp\left(\frac{\gamma_{ij}\sigma_{ij}}{r_{ij} - a_{ij}\sigma_{ij}}\right) \exp\left(\frac{\gamma_{ik}\sigma_{ik}}{r_{ik} - a_{ik}\sigma_{ik}}\right), \quad (3.3)$$

where $\theta_{0,ijk}$ is the equilibrium angle. The first term of eq. (3.3) includes an angle dependency analog to a harmonic oscillator based on a cosine angle distance from the equilibrium angle. The final two terms act again as a cut-off function by driving the potential to zero at $r_{ij} = a_{ij}\sigma_{ij}$ and $r_{ik} = a_{ik}\sigma_{ik}$ respectively.

The parameters used for the Si-Si bond modeling is displayed in table 3.1 along with an interpretation of each model parameter.

Table 3.1: Parameters for the stilliner weber potential used for intermolecular interactions in the silicon substrate.

Parameter	Value	Description
ϵ	2.1683	Individual depth of the potential well for each atom type pair/tiplets.
σ	2.0951	Distance for which the individual pair interactions has zero potential (analog to the LJ model).
a	1.80	The individual cut-off distance for each atom type pair.
λ	21.0	The overall depth of the three-body potential well.
γ	1.20	The shape of the three-body cut-off terms.
$\cos(\theta_0)$	-1/3	Cosine of equilibrium angle.
A	7.049556277	The overall depth of the two-body potential well.
B	0.6022245584	Scales the repulsion part of the two-body term.
p	4.0	The power dependency for the repulsion part of the two-body term.
q	0.0	The power dependency for the attraction part of the two-body term.
tol	0.0	LAMMPS: Option to define a different cut-off than the theoretical of $r = a\sigma$. $tol = 0$ refers to the theoretical being used.

3.1.4 Tersoff

This section is based on [[39], [31]].

The tersoff potential abandon the idea of a general n -body form and attempts instead to build the model on a more physics informed approach; The more neighbours an atom has the weaker the bonds will be. Thus it introduces the bond order (bond strength), that is environment specific and decrease with increasing bond coordination (number of neighbours for a given atom). The potential energy is taken to have the form

$$E = \sum_i E_i = \frac{1}{2} \sum_{i \neq j} V_{ij},$$

$$V_{ij} = f_C(r_{ij}) [f_R(r_{ij}) + b_{ij} f_A(r_{ij})],$$

where the total potential energy is decomposed into a bond energy V_{ij} . The indices i and j run over the atoms of the system with r_{ij} denoting the distance between atom i and j . Notice that the sum includes all combinations of i, j where $i \neq j$ meaning that the same bond is double counted which is the reason for the additional factor 1/2. The reasoning behind comes from the asymmetry of the bond order $b_{ij} \neq b_{ji}$ leading to a $V_{ij} \neq V_{ji}$. The bond energy is composed of a repulsive term f_R , arising from overlapping wave functions, and an attractive term f_A associated with bonding. f_C is simply a smooth cut-off function to increase computational efficiency. b_{ij} represent the bond order, i.e. the strength of the bonds, which depends inversely on the number of bonds, the bond angles (θ_{ijk}) and optionally the relative bonds lengths (r_{ij}, r_{jk}). Notice that an additional cut-off term a_{ij} was originally multiplied to f_R as a way of including terms that limit the range of the interactions to the first neighbour shell. These kind of limitations is already included in b_{ij} for the attractive term f_A but is often omitted for the repulsive term f_R , and we do so to by setting $a_{ij} = 1$.

The cut-off function f_C goes from 1 to 0 over a small interval range $R \pm D$ as

$$f_C(r) = \begin{cases} 1 & r < R - D \\ \frac{1}{2} - \frac{1}{2} \sin\left(\frac{\pi}{2} \frac{r-R}{D}\right) & R - D < r < R + D \\ 0 & r > R + D \end{cases}$$

which is continuous and differentiable for all r . R is usually chosen to include only the first neighbour shell. The repulsive and attractive terms f_R and f_A is modelled as an exponential function, similar to a morse potential,

$$f_R(r) = A \exp(-\lambda_1 r),$$

$$f_A(r) = -B \exp(-\lambda_2 r).$$

The novel feature of the model lies in modeling of the bond order b_{ij} which includes three-body interactions by summing over a third atom $k \neq i, j$ within the cut-off $r_{ik} < R + D$ as shown in the following.

$$b_{ij} = (1 + \beta^n \zeta_{ij}^n)^{-\frac{1}{2n}} \quad (3.4)$$

$$\zeta_{ij} = \sum_{k \neq i, j} f_C(r_{ik}) g(\theta_{ijk}(r_{ij}, r_{ik})) \exp(\lambda_3^m (r_{ij} - r_{ik})^m) \quad (3.5)$$

$$g(\theta) = \gamma_{ijk} \left(1 + \frac{c^2}{d^2} - \frac{c^2}{[d^2 + (\cos \theta - \cos \theta_0)^2]} \right). \quad (3.6)$$

In eq. (3.6) $\zeta_{i,j}$ is an effective coordination and $g(\theta)$ captures angle dependency as it is minimized at the equilibrium angle $\theta = \theta_0$.

The parameters used to model the graphene C-C bonds is summarized in table 3.2

Table 3.2: Parameters for the tersoff potential used for intermolecular interations in the graphene sheet

Parameter	Value	Description
m	3.0	Default (not used since $\lambda_3 = 0$)
γ	1.0	...
λ_3	0.0 \AA^{-1}	...
c	3.8049×10^4	Strength of the angular effect
d	4.3484	Determines the “sharpness” of the angular dependency
$\cos(\theta_0)$	-0.57058	Cosine of the equilibrium angle
n	0.72751	Power law exponent for the bond order dependency
β	1.5724×10^{-7}	...
λ_2	2.2119 \AA^{-1}	Decay of repulsion potential term
B	346.74 eV	Attractive potential term minimum at core ($r_{ij} = 0$).
R	1.95 Å	Center distance for cut-off
D	0.15 Å	Thickness of cut-off layers
λ_1	3.4879 \AA^{-1}	Decay of repulsion potential term
A	1393.6 eV	Repulsion potential term at core ($r_{ij} = 0$)

3.2 Integration

Having defined a system of particles governed by interatomic potentials we need to move the system forward in time. By solving Newtons equations of motion we effectively sample the microcanonical ensemble characterized by a constant number of particles N , volume V and energy E , hence denoted NVE. Newtons equaitons of motion read

$$m_i \frac{d^2 \mathbf{r}_i}{dt^2} = \mathbf{F}_i = -\nabla U_i \quad (3.7)$$

where i is the particle index and m_i its mass, $\mathbf{r}_i = (x_i, y_i, z_i)$ the position, t is time, $\nabla_i = (\frac{\partial}{\partial x_i}, \frac{\partial}{\partial y_i}, \frac{\partial}{\partial z_i})$ and U_i the potential energy. The potential energy is a function of the particle positions of nearby particles depending on the specefic potential in use. Since the forces defined by the potentials is conservative we expect the energy of the solution to be conserved. We can redefine eq. (3.7) in terms of two coupled first order differential equations

$$\dot{\mathbf{v}}_i(t) = \frac{\mathbf{F}}{m_i}, \quad \dot{\mathbf{r}}_i(t) = \mathbf{v}_i(t), \quad (3.8)$$

where $\dot{x} = dx/dt$ (Newton's notation) and $\mathbf{v} = (v_x, v_y, v_z)$ is velocity. Numerically we can solve the coupled equations by integrating over discrete timesteps. That is, we discretize the solution into temporal steps $t_k = t_0 + k\Delta t$ with start time t_0 and time-step Δt .

3.2.1 Velocity Verlet

A common algorithm to integrate Newton's equation of motion (as formulated in eq. (3.8)) is the *velocity verlet*. We can derive the algorithm by the use of Taylor expansions. We begin by expanding the next-step position vector $\mathbf{r}_i(t + \Delta t)$ at time t

$$\mathbf{r}_i(t + \Delta t) = \mathbf{r}_i(t) + \dot{\mathbf{r}}_i(t)\Delta t + \frac{\ddot{\mathbf{r}}_i(t)}{2}\Delta t^2 + \mathcal{O}(\Delta t^3), \quad (3.9)$$

where $\ddot{\mathbf{r}} = d^2\mathbf{r}/dt^2$ and Δt^n is simply the relaxed notation for $(\Delta t)^n$. Similar we take the expansions of the next-step velocity vector $\mathbf{v}_i(t + \Delta t)$ at time t

$$\mathbf{v}_i(t + \Delta t) = \mathbf{v}_i(t) + \dot{\mathbf{v}}_i(t)\Delta t + \frac{\ddot{\mathbf{v}}_i(t)}{2}\Delta t^2 + \mathcal{O}(\Delta t^3). \quad (3.10)$$

Finally, by taking the expansion of $\dot{\mathbf{v}}_i(t + \Delta t)$ we can eliminate the $\ddot{\mathbf{v}}_i$ -term in eq. (3.10) and simplify it as shown in the following.

$$\begin{aligned} \dot{\mathbf{v}}_i(t + \Delta t) &= \dot{\mathbf{v}}_i(t) + \ddot{\mathbf{v}}_i(t)\Delta t + \mathcal{O}(\Delta t^2) \\ \frac{\ddot{\mathbf{v}}_i(t)}{2}\Delta t^2 &= \frac{\Delta t}{2}(\dot{\mathbf{v}}(t + \Delta t) - \dot{\mathbf{v}}_i(t)) + \mathcal{O}(\Delta t^3) \\ &\Downarrow \\ \mathbf{v}_i(t + \Delta t) &= \mathbf{v}_i(t) + \dot{\mathbf{v}}_i(t)\Delta t + \frac{\Delta t}{2}(\dot{\mathbf{v}}_i(t + \Delta t) - \dot{\mathbf{v}}_i(t)) + \mathcal{O}(\Delta t^3) \\ &= \mathbf{v}_i(t) + \frac{\Delta t}{2}(\dot{\mathbf{v}}_i(t) + \dot{\mathbf{v}}_i(t + \Delta t)) + \mathcal{O}(\Delta t^3). \end{aligned} \quad (3.11)$$

By combining eq. (3.9) and eq. (3.11) and using Newton's second equation $\dot{\mathbf{v}} = \mathbf{F}_i(t)/m_i$ and $\mathbf{v} = \dot{\mathbf{r}}$ we arrive at the final scheme

$$\begin{aligned} \mathbf{r}_i(t + \Delta t) &= \mathbf{r}_i(t) + \mathbf{v}_i(t)\Delta t + \frac{\mathbf{F}_i(t)}{2m_i}\Delta t^2 + \mathcal{O}(\Delta t^3), \\ \mathbf{v}_i(t + \Delta t) &= \mathbf{v}_i(t) + \frac{\mathbf{F}_i(t) + \mathbf{F}_i(t + \Delta t)}{2m_i}\Delta t + \mathcal{O}(\Delta t^3). \end{aligned}$$

The scheme will give a local error of order Δt^3 corresponding to a global error of Δt^2 . One of the most popular ways to implement this numerically is as stated in the following steps.

1. Calculate $v_{k+\frac{1}{2}} = v_k + \frac{F_k}{2m}\Delta t$.
2. Calculate $r_{k+1} = r_k + v_{k+\frac{1}{2}}\Delta t$.
3. Evaluate the force $F_{k+1} = F(r_{k+1})$.
4. Calculate $v_{k+1} = v_{k+\frac{1}{2}} + \frac{F_{k+1}}{2m}\Delta t$

3.3 Thermostats

As we already mentioned above in Sec. 2, any kind of sliding friction involves mechanical work, some of which is then transformed into heat (the rest going into structural transformations, wear, etc.). The heat is then transported away by phonons (and electrons in the case of metallic sliders) and eventually dissipated to the environment [9].

Likewise all excitations generated in the simulations should be allowed to propagate in the system and disperse in the bulk of both sheet and substrate. Due to small simulation size these is likely to reflect back

and ‘‘pile up’’ unphysically. Thus in order to avoid continuous heating and attain a steady state the (Joule) heat must be removed at a steady state. This is very the viscous damping of the Langevin equations enter the picture. It can be difficult to set the value γ for the magnitude of this damping. The unphysical introduction of heat sink can be mitigated by some modifications he mention, which is kind of next level I guess.

3.3.1 Langevin thermostat

In order to control the temperature of the system we introduce the so-called Langevin thermostat. This is a stochastic thermostat that modifies Newton's equation of motion such that solution lies in the canonical ensemble characterized by a constant number of particles N , constant volume V and constant temperature T , hence denoted NVT. The canonical ensemble system is represented by the finite system being in contact with an infinite heat bath of temperature T . The NVT ensemble is equivalent to sampling a system in thermodynamic equilibrium where the weight of each microscopic state is given by the Boltzmann factor $\exp[-E/(k_B T)]$.

The Langevin equation is the modified version of Newton's second law for a Brownian particle. A Brownian particle is a small particle suspended in liquid, e.g. pollen or dust, named after Robert Brown (1773–1858) who was the first to observe its jittery motion. The Langevin equation describes this motion as the combination of viscous drag force $-\gamma \mathbf{v}$, where γ is a positive friction coefficient and \mathbf{v} the velocity vector, and a random fluctuation force \mathbf{R} . The Langevin equation reads

$$m \frac{d\mathbf{v}}{dt} = -\gamma \mathbf{v} + \mathbf{R} \quad (3.12)$$

where m is the particle mass. This effectively describes the particle of interest, the Brownian particle, as being suspended in a sea of smaller particles. The collision with these smaller particles is modelled by the drag force and the fluctuation force. We notice that if the fluctuation force is excluded eq. (3.12) becomes

$$m \frac{d\mathbf{v}}{dt} = -\gamma \mathbf{v} \Rightarrow \mathbf{v}_i(t) = v(0) e^{-\frac{\gamma t}{m}},$$

where the solution shows that the Brownian particle will come to a complete stop after a long time $\mathbf{v}_i(t \rightarrow \infty) \rightarrow \mathbf{0}$. This is in violation with the equipartition theorem

$$\frac{1}{2} m \langle v^2 \rangle_{eq} = \frac{k_B T}{2},$$

and hence the fluctuation force is necessary to obtain the correct equilibrium.

The following calculations are done in one dimension in order to simplify the notation. We describe the statistical nature of the collisions as a sum of independent momentum transfers

$$\Delta P = \sum_i^N \delta p_i$$

where ΔP denotes the change of momentum after N momentum transfers δp_i from the environment to the Brownian particle. We assume the first and second moments $\langle \delta p \rangle = 0$ and $\langle \delta p^2 \rangle = \sigma^2$. When N is large the central limit theorem states that the random variable ΔP has a Gaussian distribution with $\langle P \rangle = 0$ and $\langle \Delta P^2 \rangle = N\sigma^2$. If we consider the momentum change ΔP over a discrete time Δt , where the number of collisions is proportional to time $N \propto \Delta t$, the corresponding fluctuation force $R = \Delta P / \Delta t$ will have a variance

$$\langle R^2 \rangle = \frac{\langle \Delta P^2 \rangle}{\Delta t^2} = \frac{N\sigma^2}{\Delta t^2} \propto \frac{1}{\Delta t}.$$

In a computer simulation we need to pick a random force $R(t)$ from a Gaussian distribution every time-step Δt . These forces will not be correlated as long as Δt is larger than the correlation time of the forces from the molecules which we will assume for this model (I think there exist corrections for this to refer to here). With this assumption we can write the correlation function as

$$\langle R(t) R(0) \rangle = \begin{cases} \frac{a}{\Delta t}, & |\Delta t| < \Delta t/2 \\ 0, & |\Delta t| > \Delta t/2, \end{cases} \quad (3.13)$$

where a is some strength of (...?). In the limit $\Delta t \rightarrow 0$ the correlation function becomes

$$\langle R(t)R(0) \rangle = a\delta(t), \quad (3.14)$$

where δ denotes the dirac delta function. This is valid for all spatial coordinates which will all be independent of each other. Since both the drag force and the fluctuation force originate from the molecular fluid, where the drag force $-\alpha v$ is velocity dependent it is reasonable to assume that fluctuation force is independent of velocity, i.e. $\langle R_i v_j \rangle = 0$ for all cartesian indices i and j .

In the following we will attempt justify the Langevin equaiton (why it is like it is) and determine the relationship between the drag coefficient γ and the random force R .

From the Langevin equation eq. (3.12) we can compute the velocity autocorrelation function (Move to appendix?). We do this in one dimension for simplicity. We begin by multiplying by $(e^{\gamma t/m})/m$

$$\dot{v}(t)e^{\gamma t/m} + \frac{\gamma}{m}v(t)e^{\frac{\gamma t}{m}} = \frac{F}{m}e^{\frac{\gamma t}{m}},$$

and integrate from $t = -\infty$. By the use of integration by parts on the latter term on the left hand side we calculate the velocity

$$\begin{aligned} \int_{-\infty}^t dt' \dot{v}(t')e^{\frac{\gamma t'}{m}} + \frac{\gamma}{m}v(t)e^{\frac{\gamma t}{m}} &= \int_{-\infty}^t dt' e^{\frac{\gamma t'}{m}} \frac{F(t')}{m} \\ \int_{-\infty}^t dt' \dot{v}(t')e^{\frac{\gamma t'}{m}} + \left(\left[v(t')e^{\frac{\gamma t'}{m}} \right]_{-\infty}^t - \int_{-\infty}^t dt' \dot{v}(t')e^{\frac{\gamma t'}{m}} \right) &= \int_{-\infty}^t dt' e^{\frac{\gamma t'}{m}} \frac{F(t')}{m} \\ v(t) &= \int_{-\infty}^t dt' e^{\frac{-\gamma(t-t')}{m}} \frac{F(t')}{m}, \end{aligned}$$

where $e^{\frac{-\gamma t}{m}}$ plays the role of a response function. We can then calculate the autocorrelation

$$\begin{aligned} \langle v(t)v(0) \rangle &= \int_{-\infty}^t dt_1 \int_{-\infty}^0 dt_2 e^{\frac{t-t_1-t_2}{m}} \frac{\langle F(t_1)F(t_2) \rangle}{m^2} \\ &= \int_{-\infty}^t dt_1 \int_{-\infty}^0 dt_2 e^{\frac{t-t_1-t_2}{m}} \frac{a\delta(t_1-t_2)}{m^2} \\ &= \int_{-\infty}^0 dt_2 e^{\frac{t-2t_2}{m}} \frac{a}{m^2} = \frac{a}{2m\gamma} e^{-\frac{\gamma t}{m}}, \end{aligned}$$

where we used eq. (3.14) and the fact that the integration commutes with the average (we are allowed to flip the order). By comparing this with the equipartition theorem we get

$$\begin{aligned} \frac{1}{2}m\langle v^2 \rangle &= \frac{k_B T}{2} \\ \frac{1}{2}m\langle v(0)v(0) \rangle &= \frac{a}{4\gamma} = \frac{k_B T}{2} \\ a &= 2\gamma k_B T \end{aligned}$$

We notice the appereance of γ meaning that the magnitude of the fluctuations increase both with friction and temperature. Further we can integrate the velocity over time to get displacement $x(t)$ and show that the variance (show this? In appendix maybe?) is

$$\langle x^2(t) \rangle = \frac{2k_B T}{\gamma} \left(t - \frac{m}{\gamma} \left(1 - e^{-\gamma t/m} \right) \right),$$

where for $t \gg m/\gamma$ only the t -term survies yielding

$$\langle x^2(t) \rangle = 2k_B T t / \gamma.$$

In 1D, the diffusion constant D is related to the variance as $\langle x^2 \rangle = 2Dt$, meaning that this represents the einstein relation $D = \mu k_B T$ with the mobility $\mu = 1/\gamma$.

when $t \ll m/\gamma$ we use the Taylor expansion $1 - e^{-x} \approx x - x^2/2$ for $x \ll 1$ to get

$$\langle x^2(t) \rangle = \frac{k_B T}{m} t^2$$

which exactly matches the thermal velocity

$$v_{\text{th}} \frac{\langle x^2(t) \rangle}{t^2} = \frac{k_B T}{m}$$

which follows from the equipartition theorem. The finite correlation time γ/m hence describe the crossover from the ballistic regime $\sqrt{\langle x^2(t) \rangle} \propto t$ to the diffusive regime $\sqrt{\langle x^2(t) \rangle} \propto \sqrt{t}$.

Introduce the fluctuation-dissipation theorem concept earlier since this is a motivaiton for the Langeivn equation.

3.3.2 Implementing Langevin

The implementation of the Langevin equation into LAMMPS follows [40] and updates the force vector for each particle as

$$\begin{aligned} \mathbf{F} &= \mathbf{F}_c + \mathbf{F}_f + \mathbf{F}_r \\ &= -\nabla U - \gamma m \mathbf{v} + \sqrt{\frac{2k_B T m \gamma}{\Delta t}} \mathbf{h}(t) \end{aligned} \quad (3.15)$$

where \mathbf{F}_c is the conservative force computed via the usual inter-particle interactions described by the potential U , \mathbf{F}_f is the drag force and \mathbf{F}_r is the random fluctuation force where \mathbf{h} is a random vector drawn from a normal distribution with zero mean and unit variance. Notice that this generalized description of the Langevin equation deviates from the presentation in eq. (3.12) since we have added the conservative force \mathbf{F}_c , but also by the appearance of the mass in both the drag force and the fluctuation force due to the introduction of damping. It is beyond out scope to comprehend this. However, the fact that Δt now appears in the denominator for the random force variance $2k_B T m \gamma / \Delta t$ is due to the fact that we have discretized time. This in agreement with the formulation in eq. (3.13). By applying eq. (3.15) we get the refined velocity verlet scheme

$$\begin{aligned} \mathbf{v}_i(t + \Delta t/2) &= \mathbf{v}_i(t) - \frac{\Delta t}{2} \left(\frac{\nabla_i U(t)}{m_i} + \gamma \mathbf{v}_i \right) + \sqrt{\frac{k_B T \gamma \Delta t}{2m_i}} \mathbf{h}_i \\ \mathbf{r}_i(t + \Delta t) &= \mathbf{r}_i(t) + \mathbf{v}_i(t + \Delta t/2) \Delta t \\ \mathbf{v}_i(t + \Delta t) &= \mathbf{v}_i(t + \Delta t/2) - \frac{\Delta t}{2} \left(\frac{\nabla_i U(t + \Delta t)}{m_i} + \gamma \mathbf{v}_i(t + \Delta t/2) \right) + \sqrt{\frac{k_B T \gamma \Delta t}{2m_i}} \mathbf{h}_i \end{aligned}$$

with new random vector \mathbf{h}_i for each particle and each update. Notice however, that LAMMPS only apply this scheme to the particle groups with the thermostat on.

3.4 MD limitations (?)

3.5 LAMMPS

3.6 Fourier Transform (light)

Find out where to put this if nessecary.

Fourier transform is a technique where we transform a function $f(t)$ of time to a function $F(k)$ of frequency. The Forward Fourier Transform is done as

$$F(k) = \int_{-\infty}^{\infty} f(t)e^{-2\pi i k x} dx$$

For any complex function $F(k)$ we can decompose it into magnitude $A(k)$ and phase $\phi(k)$

$$F(k) = A(k)e^{i\phi(k)}$$

Hence when performing a Forward Fourier transform on a time series we can determine the amplitude and phase as a function of frequency as

$$A(k) = |F(k)|^2, \quad \phi(k) = \Im \ln F(k)$$

Chapter 4

Machine Learning (ML)

- Feed forward fully connected
- CNN
- GAN (encoder + decoder)
- Genetic algorithm
- Using machine learning for inverse designs partly eliminate the black box problem. When a design is produced we can test it, and if it works we not rely on machine learning connections to verify it's relevance.
- However, using explanations techniques such as maybe t-SNE, Deep dream, LRP, Shapley values and linearizations, we can try to understand why the AI chose as it did. This can lead to an increased understanding of each design feature. Again this is not dependent on the complex network of the network as this can be tested and verified independently of the network.

4.1 Feed forward network / Neural networks

4.2 CNN for image recognition

4.3 GAN (encoder + decoder)

4.4 Inverse design using machine learning

4.5 Prediction explanation

4.5.1 Shapley

4.5.2 Linearizations

4.5.3 LRP

4.5.4 t-SNE

Part II

Simulations

Chapter 5

Defining the system

The simulated system consists of two major parts: A 2D graphene sheet and a 3D Silicon “bulk” substrate. These parts interact with a van der Waals force (modelled by the LJ potential). We apply a normal load to the sheet inducing a normal force response between the sheet and substrate. By dragging the sheet along the substrate we measure the responding frictional forces.

Maybe include a few words about the preceding considerations between two different simulations approaches: The one that we use now and the *graphene skin* setup, where one would consider the graphene sheet as the top part of the substrate and then measure friction with an indenting tip (AFM-style). This would probably be more directed towards grasping robot applications (with ability to stretch and relax the sheet before grasping) or creation of fixed pre-stretched surfaces in the case that certain friction coefficients of interest could be achieved here.

5.1 Region definitions (Sheet, pullblocks and substrate)

The system, sheet and substrate, is further subdivided according to functionality in the MD simulations. The sheet ends is reserved for so-called *pull blocks*, which is used application of normal load, stretching and dragging the sheet, and as a thermostat, while the remaining *inner sheet* is left as an untouched (NVE) canvas for kirigami cuts. The pull blocks are equal split between a thermostat part and a rigid part which is locked into a single rigid body after an initial relaxation period. Note that the rigid part of the pull blocks on both side is considered a single rigid object even though they are physically separated. This means that all force interactions on these parts will be applied as a common average making the move in total synchronization. The substrate is equally divided into three parts: The *upper layers* (NVE) responsible for the sheet-substrate interaction, the *middle layers* being a thermostat (NVT), and the *bottom layers* is frozen (rigid and fixed) in the initial lattice structure to ensure that the substrate stays in place. In figure 5.1 the system is displayed with colors matching the three distinct roles:

1. Red: NVE parts which is governing the frictional behaviour of interest.
2. Green: Thermostats (NVT) surrounding the NVE parts in order to modify the temperature without making disturbing changes to the interaction of the sheet and substrate.
3. Blue: Parts that is initially or eventually turned into rigid objects. For the substrate this is additionally locked off and immobile.

The total system size in terms of atom count is given in table 5.1 while the sheet length dimension is given in table ??

The total system size (without cuts in the sheet) is 27456 atoms, and the distribution into the various regions is shown in table 5.1. The length dimensions of the sheet is given in table 5.2.

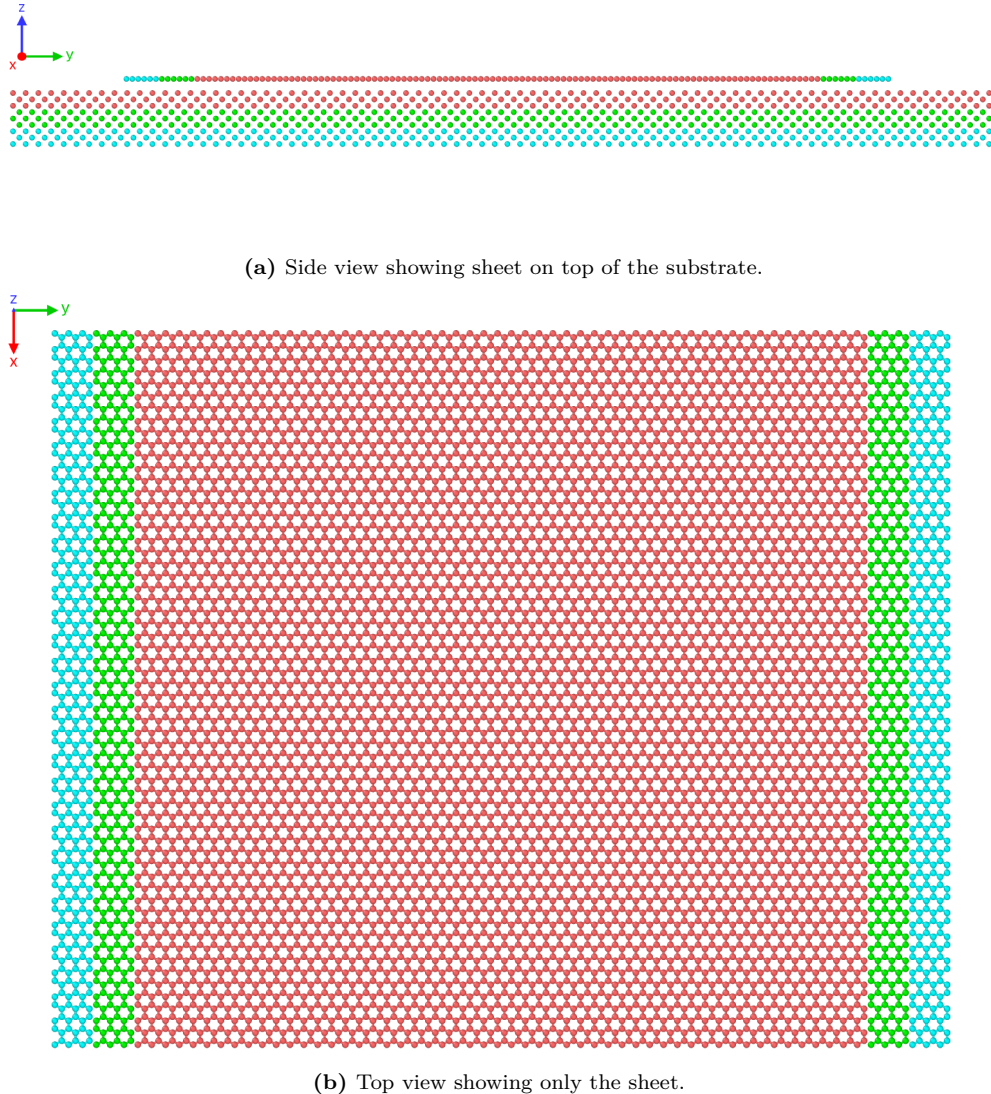


Figure 5.1: System configuration colorized to indicate NVE parts (red), thermostat parts (green) and rigid parts (blue).

Table 5.1: Amount of atoms in the various system regions in the case of no cutting applied to the sheet.

Region	Total	Sub region	Sub total	NVE	NVT	Rigid
Sheet	7800	Inner sheet	6360	6360	0	0
		Pull blocks	1440	0	720	720
Substrate	19656	Upper	6552	6552	0	0
		Middle	6552	0	6552	0
		Bottom	6552	0	0	6552
All	27456			12912	7272	7272

Table 5.2: Sheet dimensions comparing the full sheet to its subdivisions: inner sheet and pull blocks.

Group	x, y -dim	dim [Å]	Area [Å ²]
Full sheet	$x_S \times y_S$	$130.029 \times 163.219 \text{ Å}$	21,223.203
Inner sheet	$x_S \times 81.40 \%_{y_s}$	$130.029 \times 132.853 \text{ Å}$	17,274.743
Pull blocks	$2 \times x_S \times 9.30 \%_{y_s}$	$2 \times 130.029 \times 15.183 \text{ Å}$	$2 \times 1,974.230$

5.2 Numerical procedure

The numerical procedure for the friction simulations can be arranged as the following.

1. Relax (15 ps): The sheet and substrate is relaxed for 15 ps. They are both initially added in their crystalline form. The sheet is constrained under three hard spring forces (spring constant $10^5 \text{ eV/Å}^2 \sim 1.6 \times 10^6 \text{ N/m}$): One spring attaches the sheet center of mass (CM) to its original position preventing drift, while the remaining two are attached to the CM for the pull blocks to their initial position respectively to prevent rotation. These spring forces are immediately terminated after the relax phase. In this phase the pull blocks are only rigid with respect to the z-direction (perpendicular to the sheet). That is, all the forces in the z-direction are summed up and distributed on the pull blocks while it is free to expand and contract in the x-y-plane. This is mainly to ensure that it achieves the correct lattice spacing according to the temperature of the system. For the remaining phases the rigid parts of the pull block is in fact rigid with respect to all directions.
2. Stretch: The sheet is stretched by separating the rigid parts of the pullblock at constant velocity until the desired stretch amount is met.
3. Pause 1 (5 ps): The sheet is relaxed for 5 ps after the stretch procedure.
4. Pause 2 (Normal load): The normal load is applied to the rigid parts of the pull blocks together with a damping force to prevent hard impact between sheet and substrate as the separating distance is now reduced depending on the strength of the normal load. The damper is terminated after 0.5 ps, as this was suitable for the extreme load cases of our force range, and the system is relaxed until a total of 5 ps has passed.
5. Drag: A virtual atom is introduced into the simulation which exclusively interacts with the rigid parts of the pull through a spring force with variable spring constant K in the x-y-plane. The z-direction is not affected by the spring force and is governed by the balance between normal load and the normal force response from the sheet-substrate interaction. The virtual atom is immediately given a constant velocity corresponding to a variable *drag speed* parameter

At the initial timestep the three nearest neighbours (at distance 1.42 Å) of all graphene atoms are recorded. If these nearest neighbours exceed a threshold of 4 Å this raises a rupture flag which halts the simulation early. Thus, we effectively prevent any kind of wear on the sheet. For the substrate we do not perform such an analysis but only visually confirms that no wear is occurring under the most extreme simulation parameters.

5.3 Creating the sheet

We are going to create a 2D sheet graphene sheet.

5.3.1 Graphene

Graphene is a single layer of carbon atom, graphite is the bulk, arranged in a hexagonal lattice structure. We can describe the 2D crystal structure in terms of its primitive lattice vector and a basis. That is we populate each

lattice site by the given basis and translate it to fill the whole plane by any linear combination of the lattice vectors

$$\mathbf{T}_{mn} = m\mathbf{a}_1 + n\mathbf{a}_2, \quad m, n \in \mathbb{N}.$$

For graphene we have the primitive lattice vectors

$$\mathbf{a}_1 = a \left(\frac{\sqrt{3}}{2}, -\frac{1}{2} \right), \quad \mathbf{a}_2 = a \left(\frac{\sqrt{3}}{2}, \frac{1}{2} \right), \quad |\mathbf{a}_1| = |\mathbf{a}_2| = 2.46 \text{ \AA}.$$

Notice that we deliberately excluded the third coordinate as we only consider a single graphene layer on not the bulk graphite consisting of multiple layers stacked on top of each other. The basis is

$$\left\{ (0,0), \frac{a}{2} \left(\frac{1}{\sqrt{3}}, 1 \right) \right\}$$

It turns out that the spacing between atoms is equal for all pairs with an interatomic distance

$$\left| \frac{a}{2} \left(\frac{1}{\sqrt{3}}, 1 \right) \right| \approx 1.42 \text{ \AA}.$$

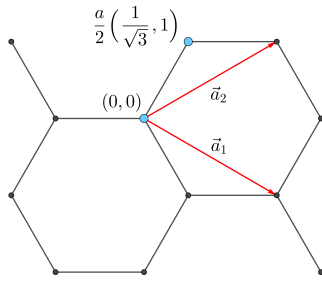


Figure 5.2: Graphene crystal structure with basis.

5.3.2 Indexing

In order to define the cut patterns applied to the graphene sheet we must define an indexing system. We must ensure that this gives an unique description of the atoms as we eventually want to pass a binary matrix, containing 0 for removed atom and 1 for present atom, that uniquely describes the sheet. We do this by letting the x-coordinate point to zigzag chains and the y-coordinate to the position along that chain. This is illustrated in figure 5.3. Other solutions might naturally involve the lattice vectors, but as these only can be used to translate to similar basis atoms a unfortunate duality is introduced as ones need to include the basis atom of choice into the indexing system. With the current system we notice that locality is somewhat preserved. That is, atom (i, j) is in the proximity of $\{(i+1, j), (i-1, j), (i, j+1), (i, j-1)\}$, but only three of them are categorized as nearest neighbours due to the hexagonal structure of the lattice. While $(i, j \pm 1)$ is always nearest neighbours the neighbour in the x-direction flip sides with incrementing y-coordinate. That is the nearest neighbours (NN) is decided as

$$\begin{aligned} j \text{ is even} &\rightarrow \text{NN} = \{(i+1, j), (i, j+1), (i, j-1)\}, \\ j \text{ is odd} &\rightarrow \text{NN} = \{(i-1, j), (i, j+1), (i, j-1)\}. \end{aligned}$$

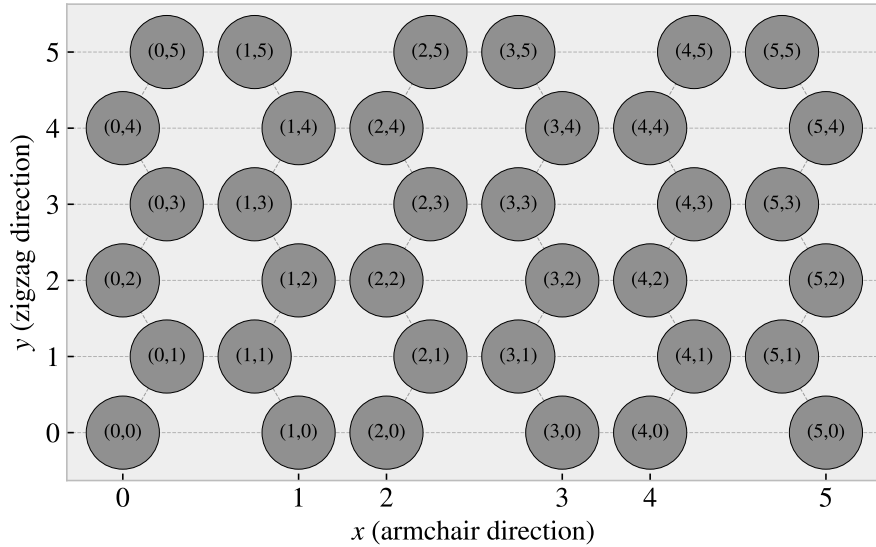


Figure 5.3: Graphene atom indexing

5.3.3 Removing atoms

As a mean to ease the formulation of cut patterns we introduce pseudo center element in each gap of the hexagonal honeycombs, see figure 5.4.

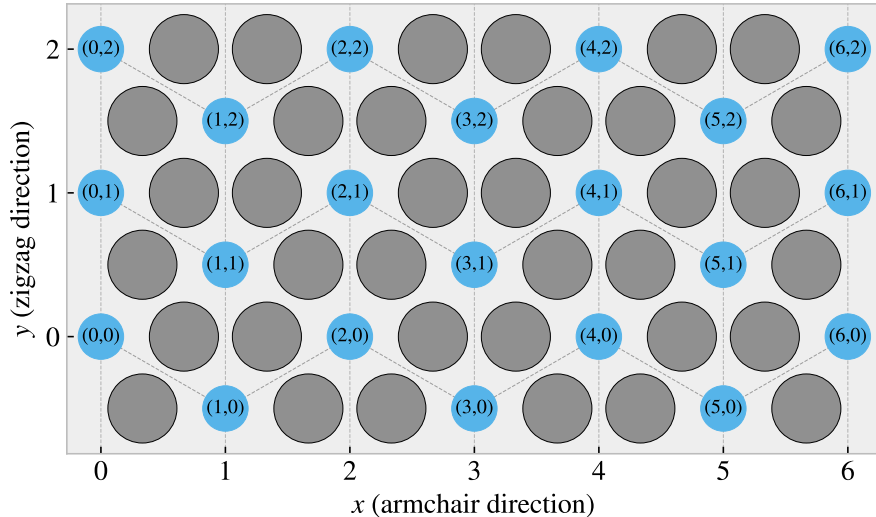


Figure 5.4: Graphene center indexing

Similar to the case of the indexing for the carbon atoms themselves the nearest neighbour center elements alternate with position, this time along the x-coordinate. Each center element has six nearest neighbours, in clock wise direction we can denote them: “up”, “upper right”, “lower right”, “down”, “lower left”, “upper left”. The “up” and “down” is always accessed as $(i, j \pm 1)$, but for even i the $(i + 1, j)$ index corresponds to the “lower right” neighbour while for odd i this corresponds to the “upper right” neighbour. This shifting applies for all left or right neighbours and the full neighbour list is illustrated in figure 5.5.

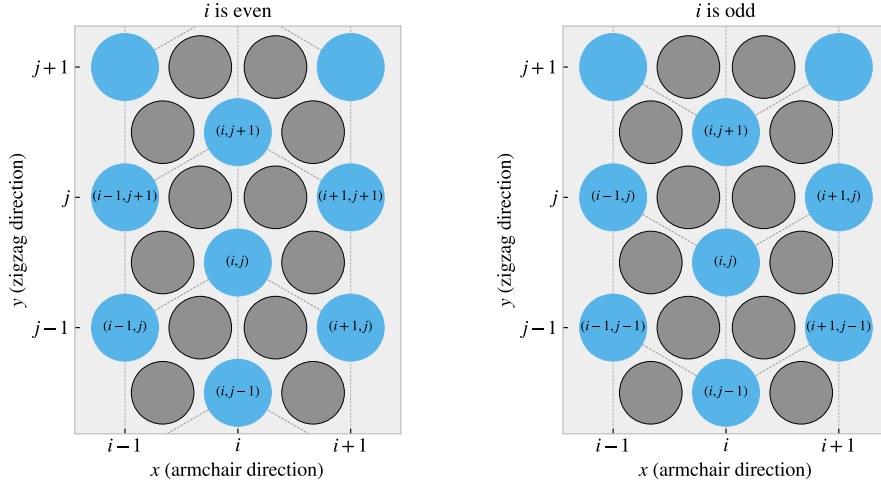


Figure 5.5: Graphene center elements directions

We define a cut pattern by connecting center elements into connected paths. As we walk element to element we remove atoms according to one of two rules

1. Remove intersection atoms: We remove the pair of atoms placed directly in the path we are walking. That is, when jumping to the “up” center element we remove the two upper atoms located in the local hexagon of atoms. This method is sensitive to the order of the center elements in the path.
2. Remove all surrounding atoms: We simply remove all atoms in the local hexagon surrounding each center element. This method is independent of the ordering of center elements in the path.

We notice that removing atoms using either of these rules will not guarantee an unique cut pattern. Rule 1 is the more sensitive to paths but we realize that, for an even i , we will remove the same five atoms following either of the following paths.

$$\begin{aligned}
 (i, j) &\rightarrow \underbrace{(i + 1, j + 1)}_{\text{upper right}} \rightarrow \underbrace{(i, j + 1)}_{\text{up}} \rightarrow \underbrace{(i + 1, j + 2)}_{\text{upperright + up}} \rightarrow \underbrace{(i + 1, j + 1)}_{\text{upper right}} \\
 (i, j) &\rightarrow \underbrace{(i + 1, j + 1)}_{\text{upper right}} \rightarrow \underbrace{(i + 1, j + 2)}_{\text{upperright + up}} \rightarrow \underbrace{(i, j + 1)}_{\text{up}}
 \end{aligned}$$

For rule 2 it is even more obvious that different paths can result in the same atoms being removed. This is the reason that we needed to define and indexing system for the atom position itself even though that all cuts generated manually will use the center element path as reference.

Illustrate some delete path?

5.4 Kirigami patterns

5.4.1 Pop-up

5.4.2 Honeycomb

5.4.3 Random walk

Chapter 6

Pilot study

Consider relabeling drag length to sliding distance instead.

6.1 Friction simulation parameters

The friction simulation is governed by a set of parameters where some is kept constant while other is varied to gain insight in the frictional properties. These parameters can be categorised into three main categories of different purpose as described in table 6.1.

Table 6.1: Parameters of the numerical procedure for measuring friction.

Category	Parameter name: description	Category purpose
Physical	<ul style="list-style-type: none"> - T: Temperature for the Langevin thermostat. - v_{slide} : Sliding speed for the sheet translation. - K: Spring constant for the spring force between the virtual atom and the pull blocks responsible for translating the sheet along the substrate. An infinite spring constant is achieved by moving the pull blocks as a rigid body (Lammps: fix move). - Scan angle: The direction for which we translate the sheet. 	Parameters expected to have a physical effect on the friction properties, which is kept fixed and thus not included in the machine learning input set.
Measurement	<ul style="list-style-type: none"> - dt: Integration timestep. - t_R: Relaxation time before stretching. - Pauses between stretch and adding normal force and between dragging the sheet. - Stretch Speed: How fast to stretch the sheet. - Slide distance: How far to translate the sheet. - Sheet size: Spatial size of the 2D sheet. - Pull block size: spatial size of the pull blocks. 	Parameters influencing the simulation dynamics and being representative of the experimental procedure that we are mimicking. These parameters are chosen with the aim of getting stable parameters under small perturbations of the given parameter.
ML input	<ul style="list-style-type: none"> - Sheet configuration: A binary matrix containing information of which atoms are removed (0) and which are still present (1) in the graphene sheet. - Stretch amount: The relative sheet stretch in percentage. - F_N: Applied normal force to the pull blocks. 	The remaining parameters serve as input variables for optimization process and is thus given as input variables for the machine learning (ML).

Due to the great number of parameters, and corresponding range of reasonable numerical values they can take, it is ... to parameter search including all of these. Thus, we will to a great extent rely on a reverse engineering in order to establish a set of parameters for the *physical* and *measurement* categories along with numerical ranges for the *ML input* category which gives stable and promising results. By doing so we effectively narrow down the parameter regime for which the investigated frictional properties belong. We aim to choose the parameters in order to accommodate a balance between generalizable and stable result which is simultaneously a suitable candidate as a proof of concept for the control of friction properties using kirigami inspired cuts.

In the following we present the results of the friction simulations in parallel to the procedure of investigating the choice of different parameters.

In the following subsections (X to Y) we are going to present the friction simulation results in parallel to the presentation of the reasoning behind the parameter choices. For this we will refer to the default parameter choice showcased in table 6.2 which is representative of the final parameter choices.

Table 6.2: Final parameters for the friction simulations Probably not the neatest format for this...

Physical	Measurements	ML input
$T = 300 \text{ K}$ $v_{\text{slide}} = 20 \text{ m/s}$ $K = \text{inf}$ (LAMMPS: <i>fix move</i>) Scan angle : $(x, y) = (0, 1)$	$dt = 1 \text{ fs}$ $t_R = 15 \text{ ps}$ Pauses = 5 ps Stretch speed = 0.01 ps^{-1} Slide distance = 400 \AA Sheet size = $130.029 \times 163.219 \text{ \AA}$ Pull block size = $2 \times 130.029 \times 15.183 \text{ \AA}$	Sheet configuration = Contiguous Stretch amount = Below rupture $F_N = [0.1, 10] \text{ nN}$

Say something about how these parameters are chosen. Reference to articles for which these were mirrored from.

6.1.1 Pressure reference for normal load domain

Find place to put this.

In order to relate the magnitude of the normal force in our friction measurement we will use the pressure as a reference. We will use the pressure underneath a stiletto shoe as a worst case for human pressure execution underneath the shoe. From (source 1) it is reported that the diameter of a stiletto heeled shoe can be less than 1 cm. Hence a 80 kg man³ standing on one stiletto heel (with all the weight on the heel) will result in a pressure

$$P = \frac{F}{A} = \frac{mg}{r^2\pi} = \frac{80 \text{ kg} \cdot 9.8 \frac{\text{m}}{\text{s}^2}}{(\frac{1 \times 10^{-2} \text{ m}}{2})^2\pi} = 9.98 \text{ MPa}$$

While this is in itself a spectacular realization that is often used in introductory physics courses (source 2) to demonstrate the rather extreme pressure under a stiletto heel (greater than the foot of an elephant) (how many Atmos?) this serves as a reasonable upperbound for human executed pressure. With a full sheet area of $\sim 21 \times 10^3 \text{ \AA}^2$ we can achieve a similar pressure of $\sim 10 \text{ MPa}$ with a normal force of

$$F_N = 10 \text{ MPa} \cdot 21 \times 10^{-17} \text{ m}^2 = 2.10 \text{ nN}$$

Of course this pressure might be insufficient for various industrial purposes, but with no specific procedure in mind this serves as a decent reference point. Notice that if we consider a human foot with area 113 cm^2 the pressure drops to a mere 70 kPa corresponding to $\sim 0.01 \text{ nN}$.

³Yes, a man can certainly wear stiletto heels.

6.2 Single friction simulation analysis

We begin by assessing the raw data for a single friction simulation run with the default parameters shown in table 6.2 for a non-cut sheet, no stretch and an applied normal force of 1 nN.

6.2.1 Force oscillations

We first assess the raw data for the friction force F_{\parallel} parallel to the drag direction as seen in figure 6.1. The sample rate is $10 \text{ ps}^{-1} = 100 \text{ timesteps}^{-1}$ for which each sample is the mean value of the 100 timesteps preceding the given sample interval. We observe immediately that the data carries oscillations on different time scales. By applying a savgol filter to the data with a polyorder of 5 and window length of 150 timesteps, corresponding to a sliding distance of 3 Å or a time window of 15 ps, we can qualitatively point out at least two different frequencies of oscillation. On figure 6.1a we see roughly three waves on the savgol filter corresponding to a relative high frequency, while on 6.1b the same savgol filter reveals a lower frequency on top of the first, creating the visual pattern of a wavepacket.

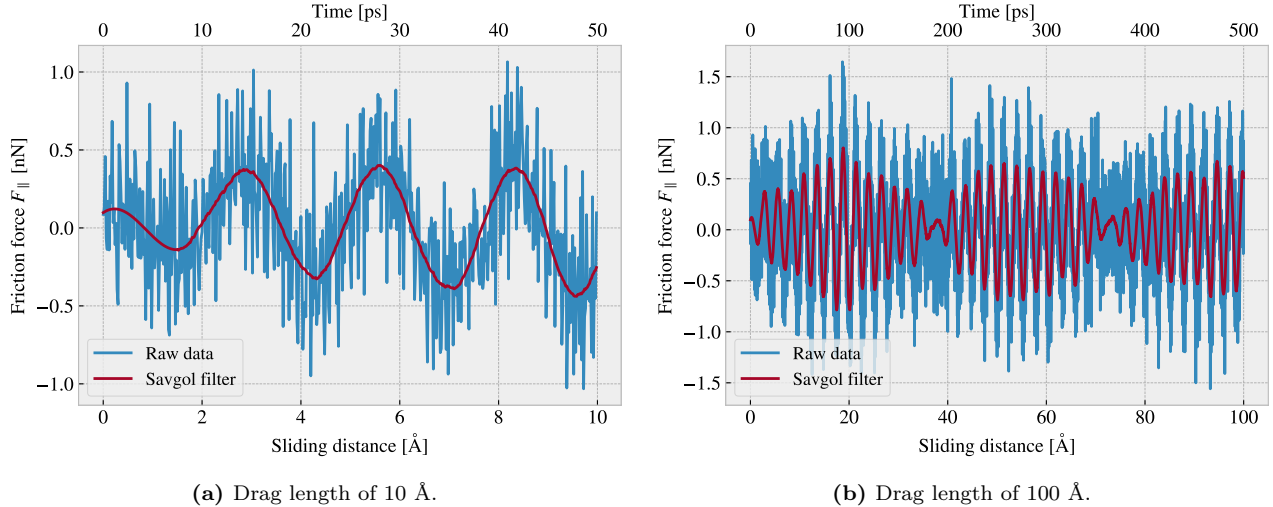


Figure 6.1: Friction force F_{\parallel} with respect to the drag direction between (full) sheet and substrate versus sliding distance. The sliding distance is measured by the constant movement of the virtual atom and not the COM of the sheet. However, we expect these measures to be fairly identical due to the fact that the pull blocks are rigidly coupled to the virtual atom. The red line represents a savgol filter with window polyorder 5 and window length of 150 timesteps (corresponding to a sliding distance of 3 Å or a time window of 15 ps).

By performing a Fourier Transform (FT) on the data we can quantify the leading frequencies as seen in figure 6.2a. By plotting the two most dominant frequencies $f_1 = 0.0074 \text{ ps}^{-1}$ and $f_2 = 0.0079 \text{ ps}^{-1}$ as $\sin(2\pi f_1) + \sin(2\pi f_2)$ we find a qualitatively convincing fit to the observed wavepacket shape as seen in figure 6.2b. By using the trigonometric identity

$$\begin{aligned}\sin(\alpha + \beta) &= \sin(\alpha)\cos(\beta) + \cos(\alpha)\sin(\beta), \\ \sin(\alpha - \beta) &= \sin(\alpha)\cos(\beta) - \cos(\alpha)\sin(\beta),\end{aligned}$$

and decomposing $f_1 = a - b$, $f_2 = a + b$ we can rewrite the sine sum as the sinusoidal product

$$\begin{aligned}\sin(2\pi f_1) \sin(2\pi f_2) &= \sin(2\pi(a - b)) \sin(2\pi(a + b)) \\ &= \sin(a)\cos(b) + \cancel{\cos(2\pi a)\sin(2\pi b)} + \sin(2\pi a)\cos(2\pi b) - \cancel{\cos(2\pi a)\sin(2\pi b)} \\ &= 2\sin(2\pi a)\cos(2\pi b),\end{aligned}$$

with

$$\begin{aligned}a &= \frac{f_1 + f_2}{2} = 0.0763 \pm 0.0005 \text{ ps}^{-1}, & b &= \frac{f_2 - f_1}{2} = 0.0028 \pm 0.0005 \text{ ps}^{-1}, \\ &= 0.381 \pm 0.003 \text{ Å}^{-1}, & &= 0.014 \pm 0.003 \text{ Å}^{-1},\end{aligned}$$

where the latter frequency is denoted with respect to the sliding distance. This makes us recognize the high oscillation frequency as a and the low frequency as b . The faster one has a period of $T_a = 2.62 \pm 0.02 \text{ \AA}^4$. This corresponds well with the magnitude of the lattice spacing and especially that of graphene at 2.46 \AA as expected theoretically (make reference to theory section?). We also take note of the longest period $T_b = 71 \pm 15 \text{ \AA}^{-1}$ which will be relevant for the evaluation of measurement uncertainty in section 6.3.

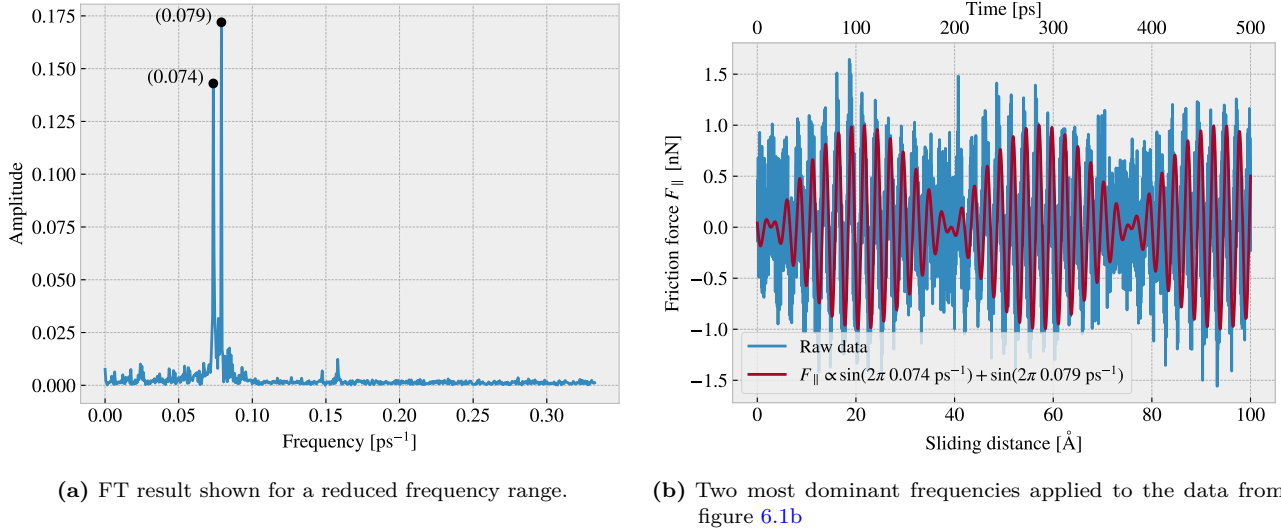


Figure 6.2: Fourier transform (FT) analysis of the full friction force data (all 400 \AA sliding distance) shown in figure 6.1. (a) shows the two most dominant frequency peaks. Note that no significant peaks were found in a higher frequency than included here. (b) shows a comparison between the raw data and the wavefunction corresponding to the two peaks in figure (a).

6.2.2 Decompositions

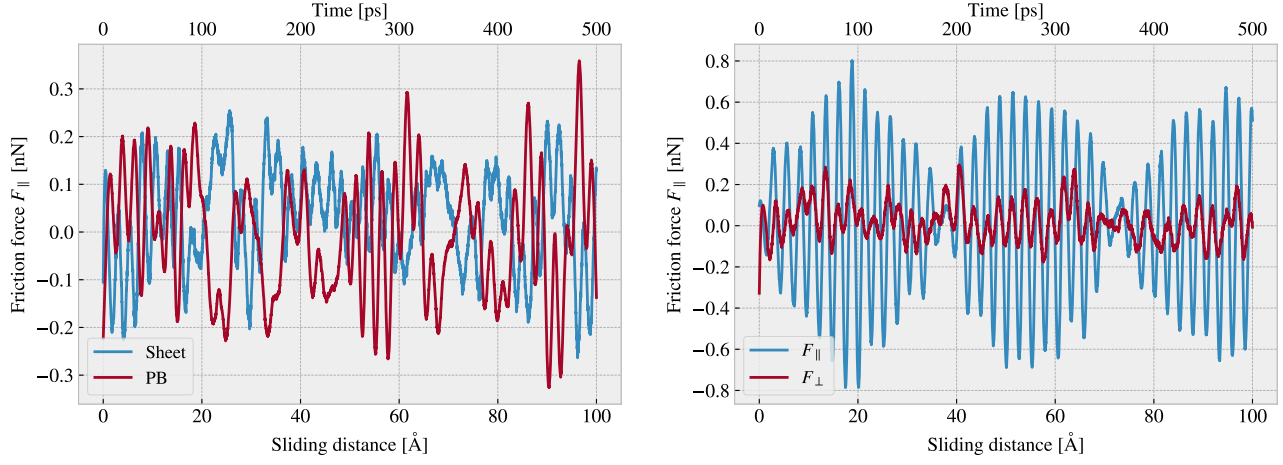
In the previous analysis we have looked only at the friction force for the full sheet, including the pull blocks which is locked off during sliding, and with respect to the drag direction. This represents our choice measurement which we will address in the following.

Due to the fact that we are only applying cuts to the inner sheet (excluding the pull blocks), it might seem more natural to only consider the friction on that part. If the desired frictional properties can be achieved by altering the inner sheet one can argue that any opposing effects from the pull blocks can be mitigated by scaling the relative size between the inner sheet and the pull blocks. However, when looking at the time series of the friction force decomposed with respect to the inner sheet and pull block region (see figure 6.3a), we observe the friction force arising from those parts are seemingly antisymmetric. That is, the distribution of the frictional pull from the substrate on the sheet is oscillating between the inner sheet and the pull block. Keeping in mind that normal force is only applied to the pull blocks we might take this as an integrated feature of the system which does not necessarily disappear when changing the spatial ratio between inner sheet and pull block. Any interesting friction properties might depend on this internal distribution of forces. Hence, we hedge our bets and use the full sheet friction force as a holistic approach to this measurement problem.

Similar we might question the decision of only considering the frictional force projected onto the sliding direction as we are neglecting the “side shift” induced during the slide phase. In figure 6.3b we see the decomposition into force components parallel F_{\parallel} and perpendicular F_{\perp} to the slide direction respectively. We see that the most dominant trend is projected into the parallel component. If we want to include the perpendicular component as well we would have to evaluate the friction as the length of the force vector for which we would lose the sign of the force direction. Hence, we would only get a positive contribution which would not be able to capture the change between resisting and assisting the sliding during stick-slip motion. One option to accommodate this is by using the vector length but keeping the sign from the projection parallel to the sliding direction. However,

⁴The uncertainty Δy is calculated as $\Delta y = \left| \frac{\partial y}{\partial x} \Delta x \right|$ for uncertainty Δx and $y(x)$

we omit such compromises as this might make analysis interpretation more difficult, and we use only the parallel component going forward.



(a) Decomposition into group inner sheet (sheet) and pull blocks (PB). (b) Decomposition into parallel (F_{\parallel}) and perpendicular (F_{\perp}) to drag sliding direction.

Figure 6.3: Friction force decomposition on the data shown in figure 6.1 with applied savgol filters similar to that of figure 6.1b with window polyorder 5 and window length of 150 timesteps (corresponding to a sliding distance of 3 Å or a time window of 15 ps).

6.2.3 Center of mass path

From the previous observations of the friction force time series we see evidence of a stick-slip behaviour. Specially, we see in figure 6.3b that this might be the case both parallel and perpendicular to the sliding direction. By looking at the x, y -position for the sheet center of mass (COM) we observe the stick-slip motion manifested as a variation in COM speed combined with a side to side motion as shown in figure 6.4a. In an attempt to increase the magnitude of the slips we evaluate a similar simulation with spring constant $K = 30 \text{ N/m}$ (see figure 6.4b) in contrast to that of an infinite spring constant. While the maximum slip speed stays within a similar order of magnitude the slip length in the sliding direction is increased along with the side to side motion. Note that the axis scale is different between figure 6.4a and 6.4a. However, in both cases we observe that the side to side motion is associated with a low speed, meaning that is more reminiscent of a “slow” creep alignment with the substrate than a slip.

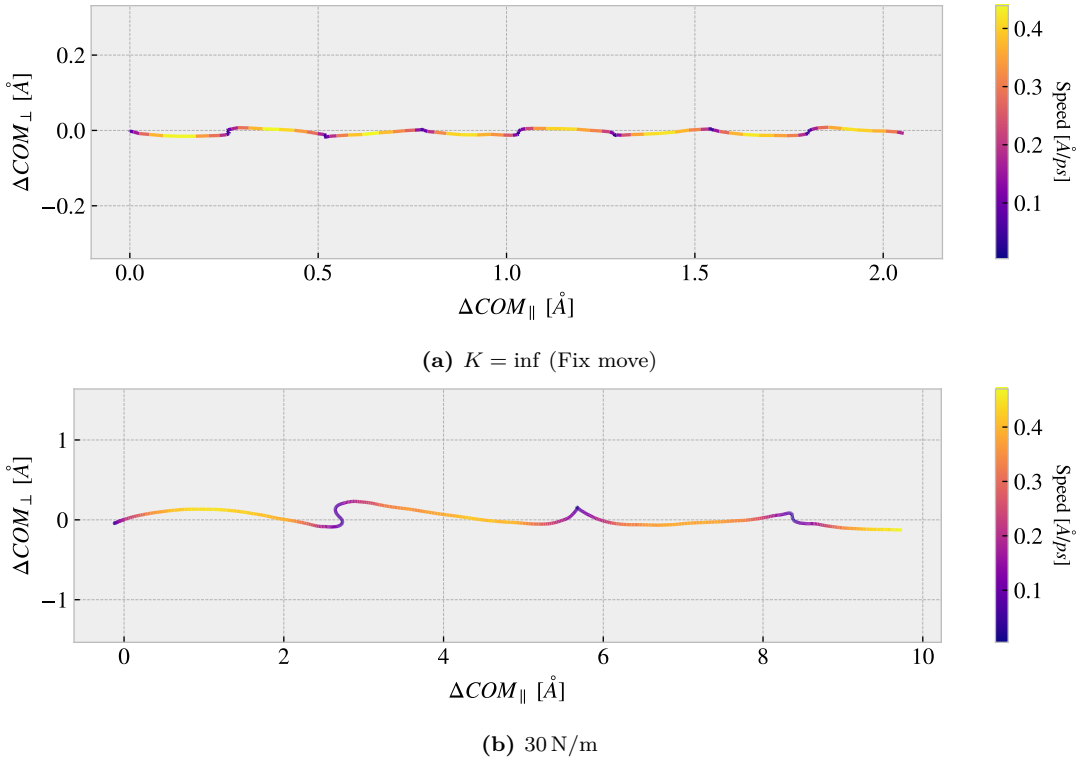


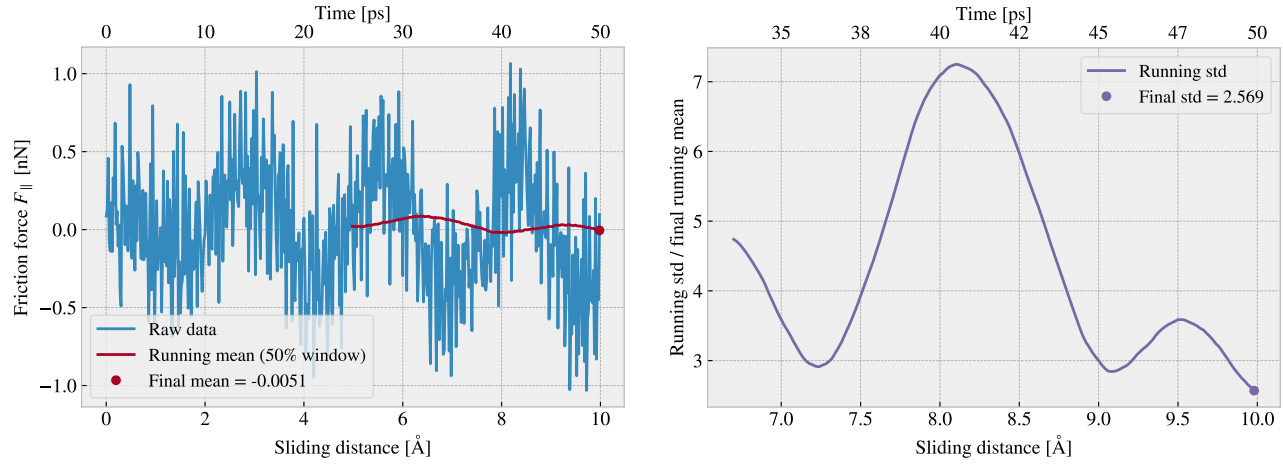
Figure 6.4: Center of mass position relative to the start of the sliding phase in terms of the direction parallel to the sliding direction ΔCOM_{\parallel} and the axis perpendicular to the sliding direction ΔCOM_{\perp} . The colorbar denotes the absolute speed of the COM.

6.3 Defining metrics for dynamic and static friction

In order to evaluate the frictional properties of the sheet we reduce the comprehensive friction force time series addressed in section 6.2 into single metrics describing the dynamic and static friction. The natural choice is to use the mean and max values of the time series.

6.3.1 Dynamic friction

For the dynamic friction measurement we take the mean value of the latter half of the dataset to ensure that we are sample from a stable system. For a full sliding simulation of 400 Å we thus base our mean value on the latter 200 Å of sliding. In figure 6.5a we have shown the friction force of the first 10 Å of sliding together with a running mean with window length of 5 Å corresponding to 50% the data length. This is merely done to illustrate the sampling procedure and by only using a 10 Å sliding distance the final mean estimate (indicated with a dot) takes a negative value due to the specific cut-off of the few oscillations captured here. Nonetheless, one approach to quantify the uncertainty of the final mean estimate is to consider the variation of the running mean preceding the final mean value. The more the running mean fluctuates the more uncertainty associated with the final estimate. However, only the running mean “close” to the ending should be considered, since the first part will rely on data from the beginning of the simulation. From the Fourier analyse in section 6.2.1 we found the longest significant oscillation period to be $\sim 71 \text{ \AA}^{-1}$ corresponding to $\sim 35\%$ of the running mean window consisting of 200 Å of slifing when including all the data. Hence, we use the standard deviation of the final 35% of the running mean to approximate the uncertainty of the final mean value, and we estimate the relative error by dividing the standard deviation by the final mean value. In figure 6.5b we showcase a running standard deviation of a window length 35% the running mean window in figure 6.5a for the illustrative case of a total 10 Å slide. The final uncertainty value is marked by a dot, and we see as expected that we get a high relative error of $\sim 257\%$ which corresponds well with the short sampling period and the mean value taking an unphysical negative value.



(a) Running mean with window length 5 Å (50% the data length). (b) Running std with window length 1.75 Å (35% the mean window length.)

Figure 6.5: Running mean and running standard deviation (std) on the friction force data from a 10 Å of sliding simulation. The running mean window is 50% the data length while the running std window is 35% the running mean window length.

When including the full dataset of 400 Å of sliding, such that std window actually matches with the longest period of oscillations expected from the data, we get a final relative error of $\sim 12\%$ as shown in fig 6.6. This is arguable just at the limit for an acceptable error, but as we shall see later (Make a reference to fig or sec) this high relative error is mainly connected to the cases of low friction. When changing the simulation parameters, such that the mean friction evaluates to considerable higher values, the relative error drops to the order (put in numbers). One interpretation of this finding is simply that the oscillations in the running mean is somewhat independent of the magnitude of the friction. In that case, the relative error will spike for the low friction cases.

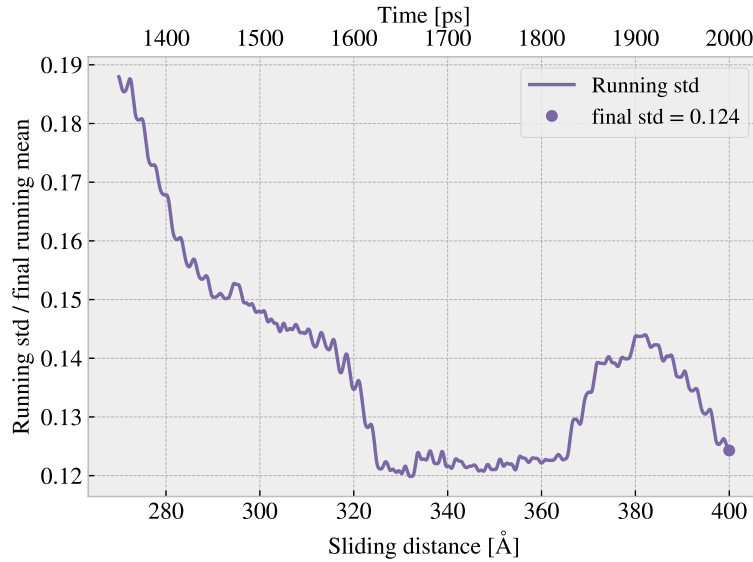


Figure 6.6: Running standard deviation (std) for a full 400 Å sliding simulation. The running std window is 70 Å (35% the running mean window of 50% the data length).

6.3.2 Static friction

The max value is the most obvious choice for addressing the static friction, even though that the definition of the static friction is a bit vague. When considering the friction force time series in figure 6.1 we observe that

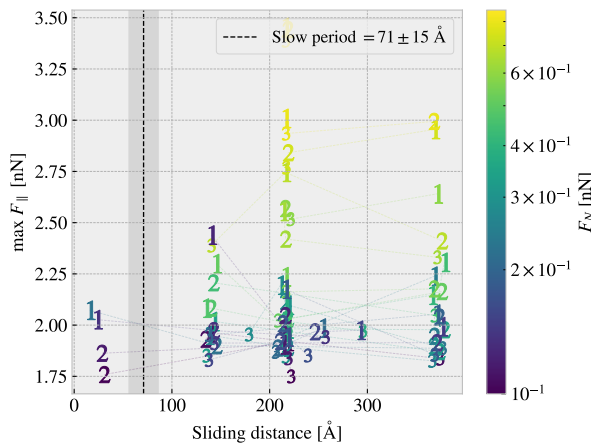


Figure 6.7: Distribution of top three max friction force peaks for 30 uniformly sampled normal forces $F_N \in [0.1, 10]$ nN. The dotted line and the grey area marks the slowest significant oscillation period found in the data and thus marking a dividing line for whether a peak falls within the “beginning” of the sliding simulation.

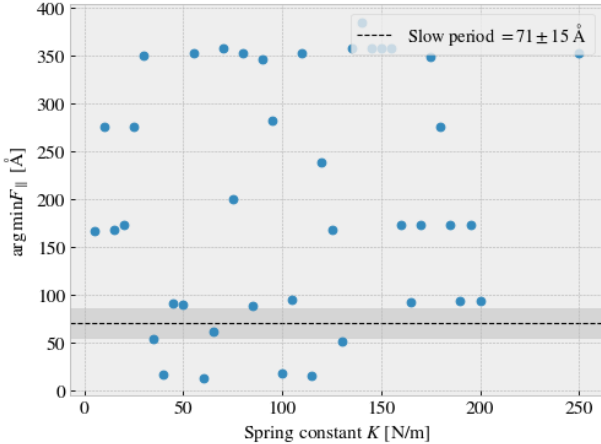


Figure 6.8: Sliding displacement for the max friction peak to appear as a function of spring constant. Fixmove is tmp mapped to $K = 200$ here without any discontinuous lines.

the stick-slip oscillations increase in magnitude toward a global peak at ~ 20 Å. Thus, we could identify this peak as the static friction force, but the global max does in fact rarely fall within the first part of the sliding. In figure 6.7 we investigate the top three max value, at which sliding distance they occur and at what magnitude, for 30 uniformly sampled normal forces in the interval [0.1, 10] nN. It is immediately clear that only few of the peaks fall within the “beginning” of the simulation defined by the slowest significant oscillation period of 71 ± 15 Å. In fact only 2/30 global values and 4/90 top three values can be associated to the start of the sliding by this definition. Thus, this result suggests that the max value cannot be used as a reliable measure for the static friction either due to its lack of presence or due to the simulation setup procedure. For a more typical evaluation of the static friction force one would increase force slowly until the first slip significant slip is recorded (a series of precursors is expected to precede this). In our simulations we drag the sheet relatively fast in a rigid manner which might be the reason for the lacking the static friction. Bonelli et al. [25] reported that the stick-slip behaviour was only presented when using a relatively soft spring. Thus, by changing the spring constant we investigate possibility to observe a static friction (**I kind of interchanged stick-slip and static friction int his argument, but I still think it can be used to argue for doing the test...**) response within the framework of our simulation procedure as shown in figure 6.8. However, the results do not indicate any implications that a recognizable domain exist for which the static friction response would be reliable. Hence, we will base the final assessment on frictional properties purely on the dynamic friction force.

6.4 Out of plane buckling

The out of plane buckling is the main motivation for applying the kirigami inspired cuts to the sheet. Thus, we perform a stretch simulation in a low temperature $T = 5$ K vacuum in order to verify that the chosen cut configurations do in fact contribute to a significant out of plane buckling when stretched. For the non-cut, popup and honeycomb configuration we assess the movement in the z-direction (perpendicular to the plane) during the stretch, which we visualize by the min and max z-value along with the atom count quartiles 1%, 10%, 25%, 50% (median), 75%, 90% and 99% as shown in figure 6.9. We observe that the popup and honeycomb pattern buckle considerably out of plane during the stretch in comparison to the non-cut sheet which only exhibit minor buckling of ~ 2 Å which is on the same order as the atomic spacing in the sheet. We also notice that the popup pattern buckles more in consideration to the min and max peaks while the 1%, 99% quartiles is on the same

magnitude as the honeycomb. By looking at the simulation visualization (**include OVITO figures for vacuum stretch as well?**) we can conclude that this is mainly due to the fringes of the sheet “flapping” around.

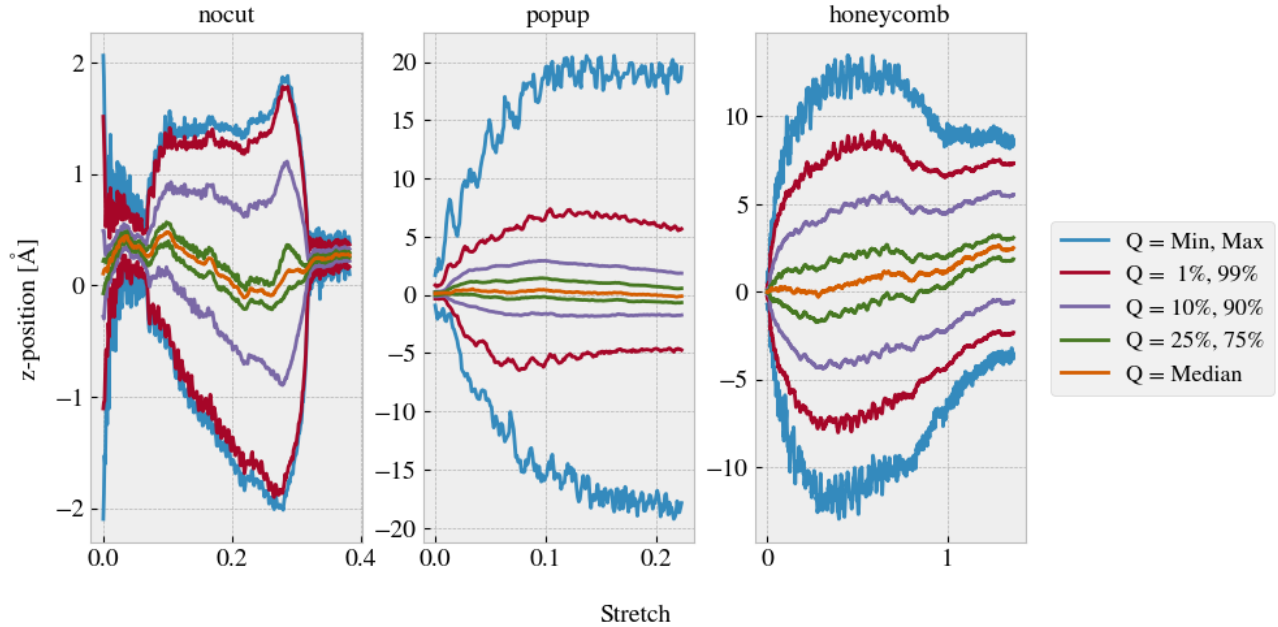


Figure 6.9: Out of plane buckling during stretch of sheets in vacuum at $T = 5$ K. Reading from left to right the vacuum rupture stretch are 0.38, 0.22 and 1.37. **perhaps use a color scale instead of the standard color cycles here.**

The next step is to verify that the buckling will lead to a significant altering of the contact area when the sheet is in put in contact with the substrate. We investigate this by simulating the stretch at the default temperature $T = 300$ K with the presence of contact forces between the sheet and substrate. Note that no normal load is applied as the sheet and substrate is sufficiently attracted by the LJ potential. Selected frames from the simulation is shown in appendix ???. We assess the contact area by the relative amount of atoms in the sheet within chemical range of the substrate. The cut-off for this interaction is 4 Å corresponding to $\sim 120\%$ the LJ equilibrium distance. Since the contact area is usually calculated as the amount of atoms in contact multiplied with an associated area for each contact this feature is taken to be proportional to the contact area. The relative amount of bonds as a function of stretch for the various configurations is shown in figure 6.10 which clearly indicates a drop in contact area as the cutted sheets are stretched.

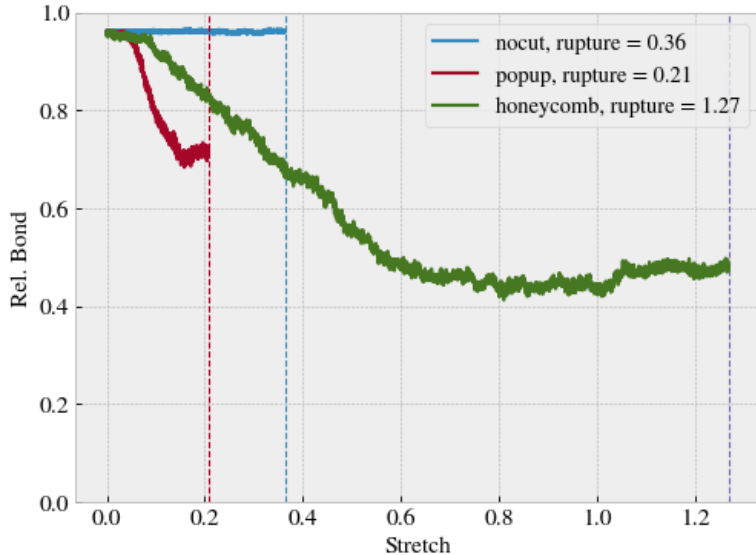


Figure 6.10: Contact vs. stretching of the sheet, where the contact is measured by the relative amount atoms in the sheet within chemical interaction range to the substrate. The cut-off for this interaction range is 4 Å corresponding to $\sim 120\%$ the LJ equilibrium distance. $T = 300$ K

Compare figure 6.10 to that of figure 6.15 where multiple simulations constitute the stretch-contact curve.

6.5 Investigating selected parameters

We investigate the importance of the physical variables T , v_{slide} and K (make plots for scan angle as well?) and the choice of timestep dt . This is done partly understand how the dependencies relate to theoretical, numerical and experimental results, and partly to understand how these parameter choices defines the regime for our multi configurational search. We use the default parameters in table 6.2 with exception of the single parameter of interest which is varied in a reasonable range of the default choice. In figure 6.11-6.14 the dynamic friction estimate and the max friction force is shown as a function of T , v_{slide} , K and dt respectively. For the dynamic friction estimate the absolute error is denoted by a shaded error which linearly connects the points.

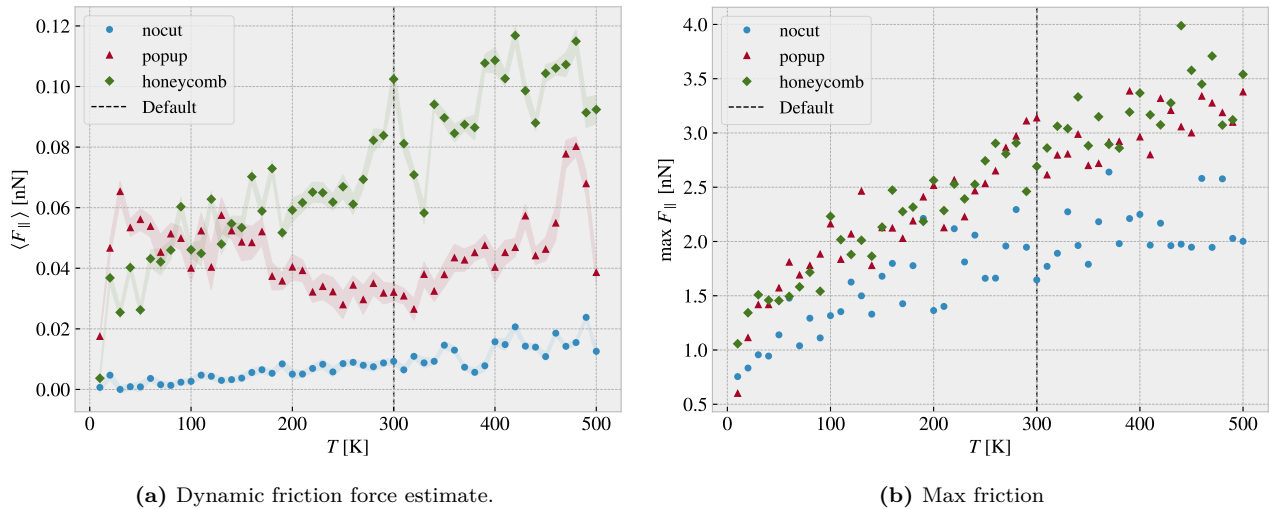


Figure 6.11: Temperature.

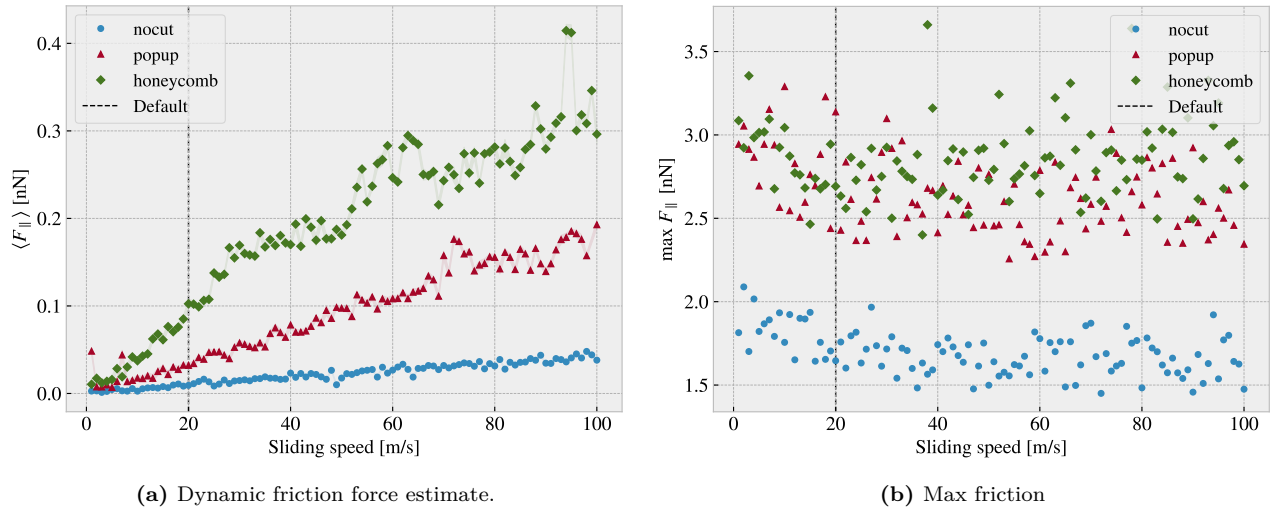


Figure 6.12: Sliding speed

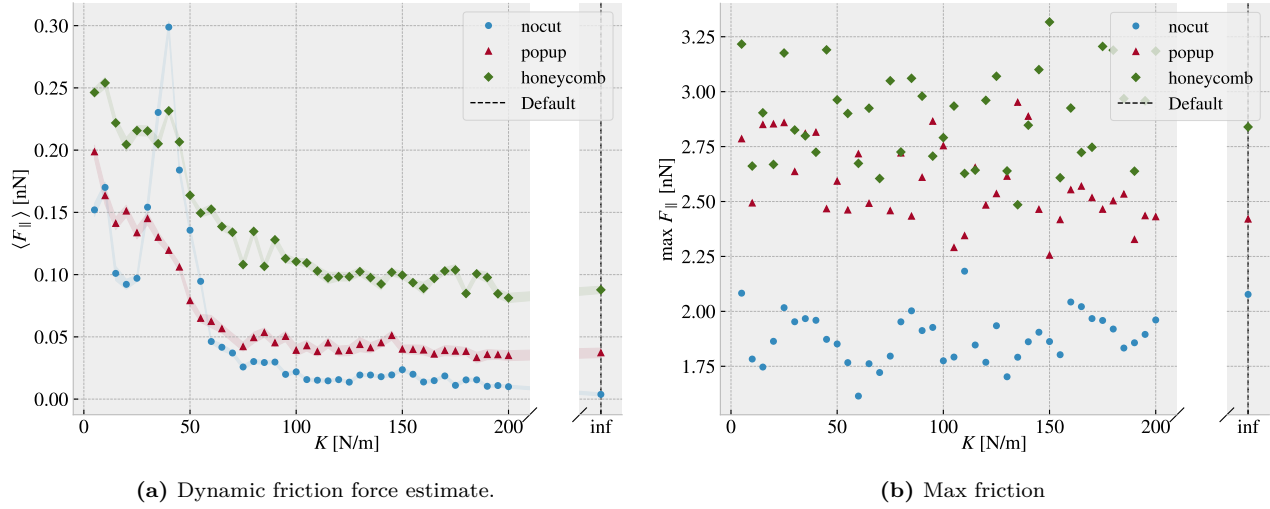


Figure 6.13: Spring constant

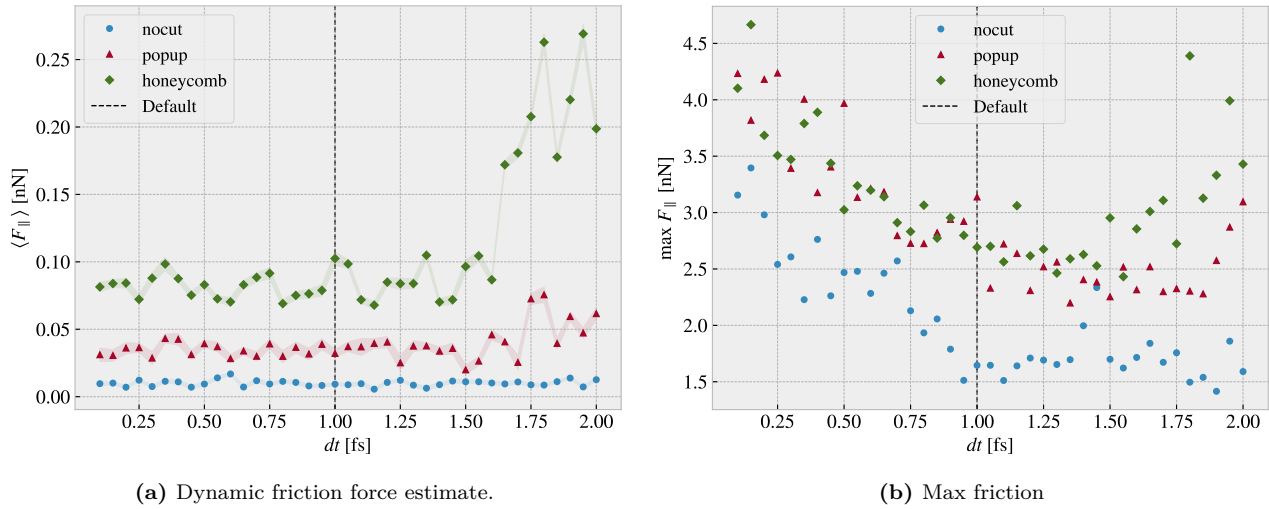


Figure 6.14: Timestep

Quick thoughts:

- Temperature: We do clearly not see the $1/T$ temperature decrease. The non-cut sheet seems to showcase a linear relationship which is also somewhat present for the honeycomb which matches some of the findings in other MD simulations. For the popup we do see a local decrease at low temperatures which flip at around the default $T = 300$ K temperature. The max friction peaks seem to increase with temperature as well indicating that the peaks might be associated with thermal fluctuations rather than actual stick-slip behaviour. This supports the finding that the static friction response is not significantly present in these simulations.
- Velocity: Considering the non-cut sheet first the velocity dependency is seemingly linear which deviates from the expected logarithmic trend. For the cutted configurations we find some peaks which might indicate the presence of resonance frequencies. The cutted sheet might be closer to a logarithmic trend, but this is not spot on either. The max friction seems to decrease slightly with small velocities and then stay rather constant. This can probably be explained by the reduced time to stick between stick slip.
- Spring constant: On all three configurations the dynamic friction decreases with an increasing spring constant. The best explanations might be due to the lack of freedom to “get stuck” in incommensurable configurations. We also notice that the friction varies a lot at lower spring constants supporting the choice of having a stiff spring for stability reasons. Especially the non-cut sheet peaks at $K = 40$ N/m. The max friction seem to be constant with K .
- dt : The dynamic friction is relatively stable around the default choice of $dt = 1$ fs. However, the fluctuations with respect to dt is more significant for popup pattern and even more for the honeycomb pattern. This indicates that the more complex dynamics of the simulation is more sensitive to the timestep. We might interpret this information as an additional measure of uncertainty. The maximum friction decreases with increasing timestep which can be asserted a statistical interpretation: Higher peaks will be captured by the high resolution of a low dt and vice versa. The high max values towards the point of $dt = 2$ fs is most likely due to the approach of instability in the simulation as seen more clearly for the dynamic friction evaluation.

6.6 Normal force and stretch dependencies

Till this point we have only changed variables one by one to investigate single dependencies. We now advance the study to a simultaneous variation of stretch and normal force.

Explain how the stretch is uniformly sampled within equally divided intervals and the normal force is actually uniformly sampled in a given range. Argue that the first might be approximately uniformly distributed for large numbers.

Talk about rupture test also. Maybe in the theory/method section under numerical procedure: Before simulating a rupture test is perform to determine under what stretch the sheet ruptures. This is a slightly higher threshold than when applied normal load and sliding along the substrate.

6.6.1 Contact area

??

We reproduce the contact area investigation of figure 6.10 with the modification that the contact count is measured as an average of the latter 50% of the sliding simulation at a non-zero applied normal load. The results are shown in figure 6.15 with 30 attempted (some rupture) stretch (pseudo) uniformly distributed stretch between 0 and the rupture point and 3 uniform distributed normal loads in the interval [0.1, 10] nN.

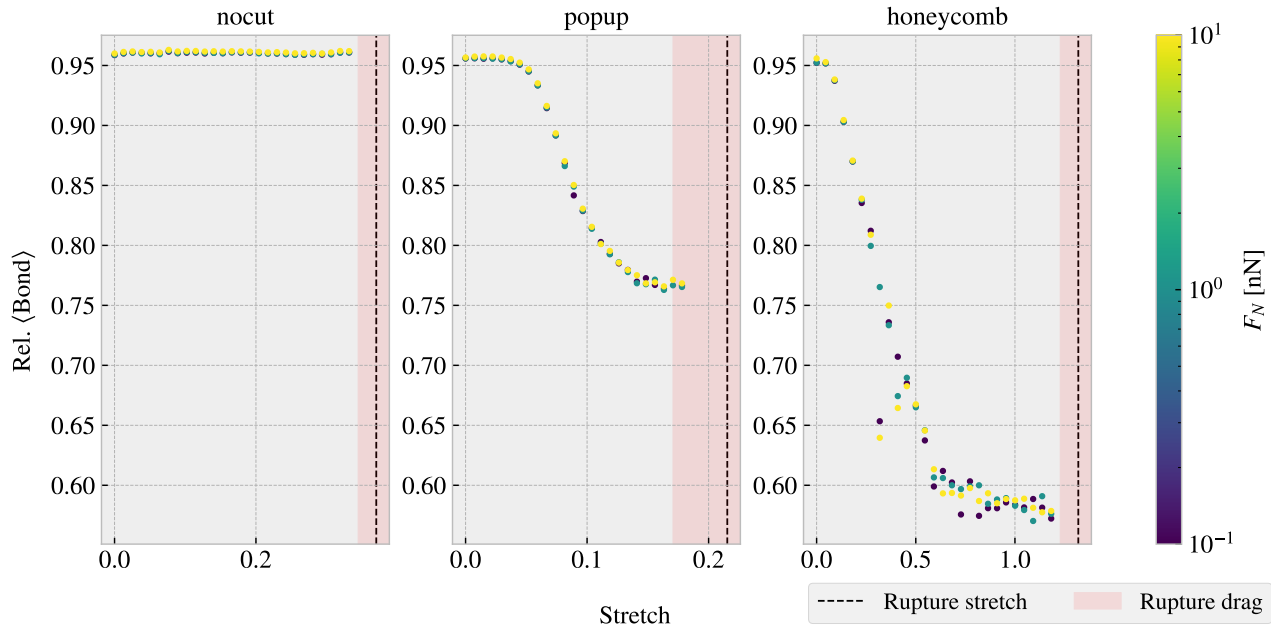


Figure 6.15: Average relative amount of bonds between the sheet and the substrate defined by the cut-off distance of 4 Å. The average is taken over the latter half of the sliding phase. The red shade denotes the stretch range where ruptures occur at certain normal loads under sliding while the black-dotted line represents the rupture point due to stretching (rupture test)

From figure 6.10 we observe a significant decrease in the contact due to stretching of the cut configurations in contrast to the non-cut which stays roughly constant. This is reminiscent of the non-sliding stretch vs. contact curve shown in figure 6.10. Given these results, theoretically one would expect the dynamic friction to decrease with stretch for the cut configurations.

6.6.2 Stretch

We make a similar analysis as done in the previous section ?? with the substitution of friction force instead of contact (The data is taken from the same simulations runs). The dynamic friction force (put uncertainty here even though that it is quite low?) and the max friction is shown in figure 6.16a and 6.16 respectively.

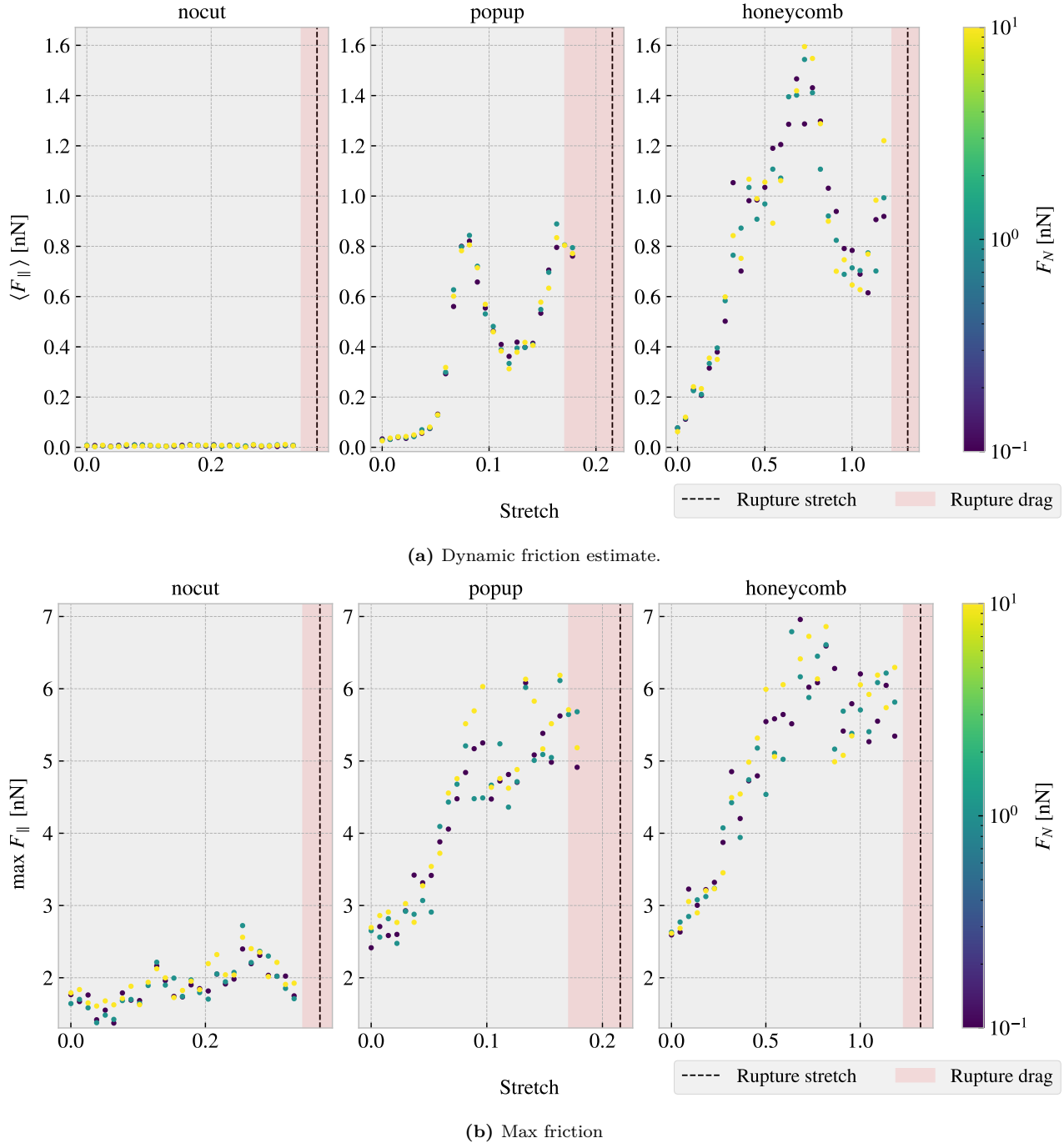


Figure 6.16: CAPTION

From figure 6.16a we find to our surprise that the dynamic friction increase with stretch for the cut configurations despite a simultaneous decrease in contact area as shown in figure 6.15. This suggests that the amount of chemical bonding atoms is not the dominant mechanism for the friction of this system. Instead, we might point to a mechanism more mechanical of nature associated to phonon excitations. When the cut sheet is stretched the stress (show stress maps somewhere or not necessary?) might induce a certain distribution and magnitude of point pressures to favor energy dissipation. Nonetheless, the results showcase a strong coupling between stretch and friction force, also for the max friction force, which is beyond the expectations at this stage of the study. The non-cut configuration does not show significant dependency on the stretch which reveal that this effect is only present when combining cut and stretch and not purely by stretching the sheet.

By considering the increase in dynamic friction towards the first peak we get a relative friction increase and increase vs. stretch ratios as described in table 6.3. While the honeycomb force increase towards the first peak is approximately linear the popup exhibits seemingly exponential growth which yield a slope on the order ~ 30 nN.

Table 6.3: (stretch, dynamic friction) coordinates from figure 6.16a at start and the first peak respectively used to approximate the relative increase in friction force and the ratio for friction increase vs. stretch for sait range. In practice the latter ratio denotes the slope of a forced linear trend.

Configuration	Start	First peak	Relative increase	Friction force vs. stretch ratio [nN]
Popup	$\sim (0, 0.03)$	$\sim (0.082, 0.83)$	27.7	9.76
Honeycomb	$\sim (0, 0.07)$	$\sim (0.728, 1.57)$	22.4	2.06

Additionally, we notice that both the popup and honeycomb also exhibits stretch ranges where the dynamic friction force decrease with increasing stretch. Qualitatively we assign the slope to be on the same order of magnitude as those towards the first peak. This is useful for the prospect of taking advantage of this phenomena as we can essentially achieve both higher and lower friction for increasing stretch for different starting points.

6.6.3 Normal force

Main take away from this section should be that the normal force does not really change the friction much; The friction coefficient is extremely low, but I'm not sure how well the linear fits are (whether they are linear or sublinear). Not sure if I should do a linearly increasing normal force for better linear plots?

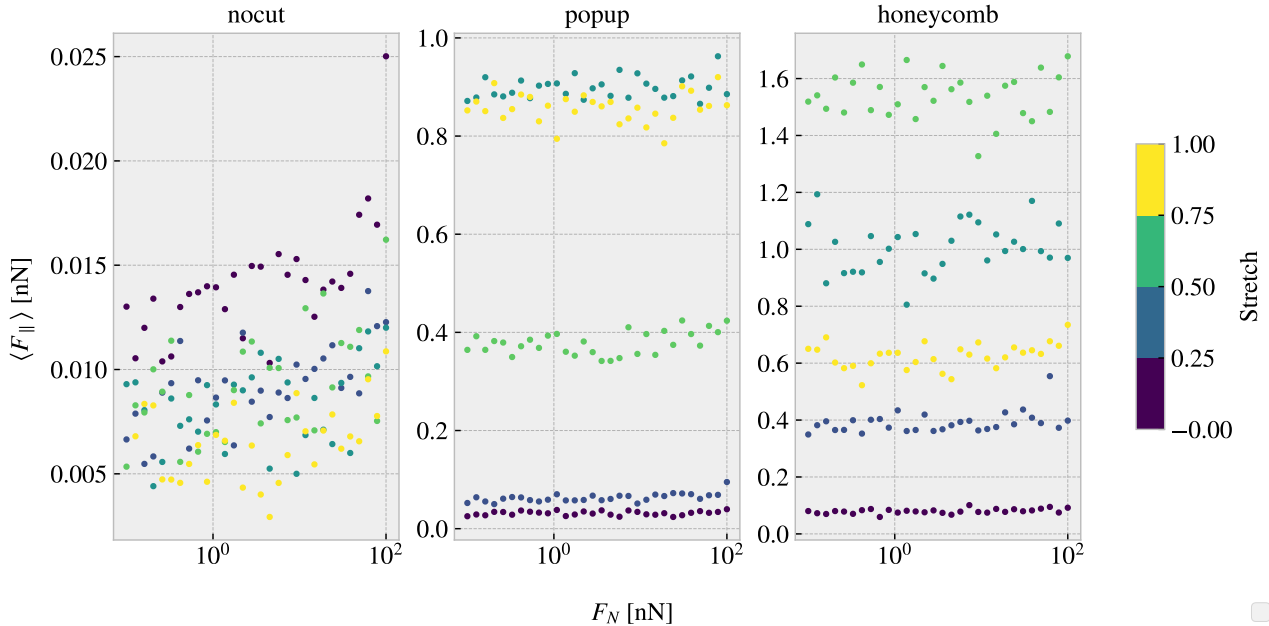


Figure 6.17: ...

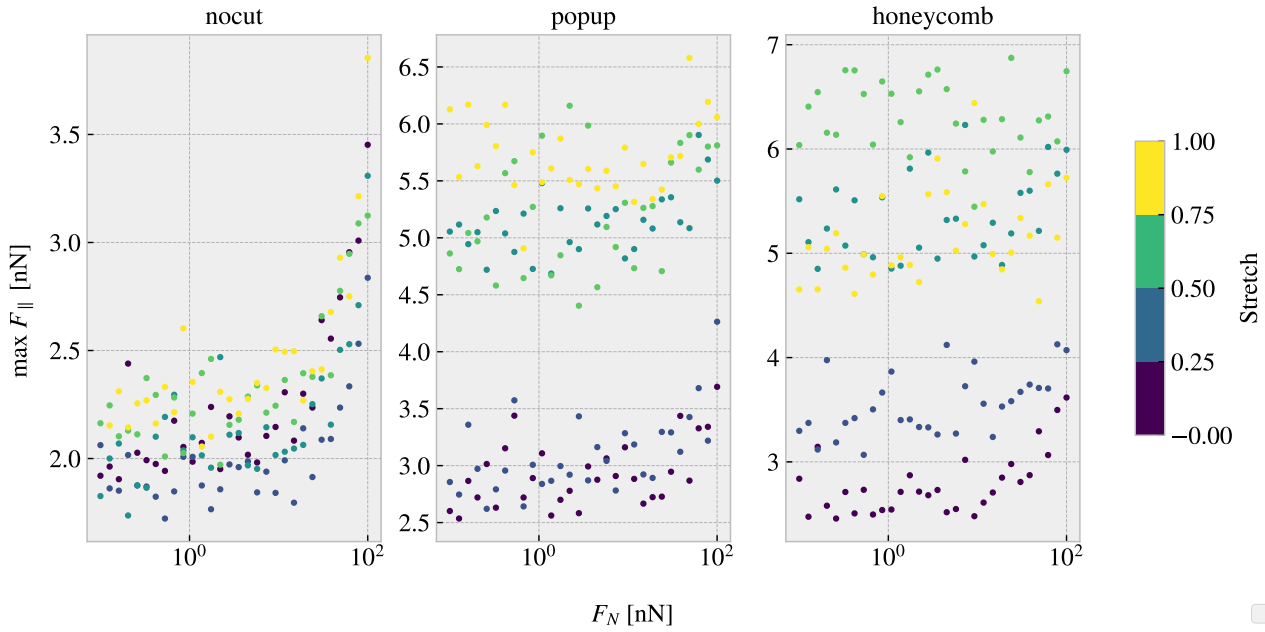


Figure 6.18: Colorbar is only fitted for the right plot (honeycomb)... this should be fixed. Should I have run a linear distribution of FN so I could plot it linear here also...?

Table 6.4: Mean friction coeff

nocut	$0.00009 \pm 1 \times 10^{-5}$	$0.00005 \pm 1 \times 10^{-5}$	$0.00004 \pm 1 \times 10^{-5}$	$0.00005 \pm 2 \times 10^{-5}$	
popup	$0.00005 \pm 3 \times 10^{-5}$	$0.00024 \pm 5 \times 10^{-5}$	$0.0002 \pm 2 \times 10^{-4}$	$0.0005 \pm 1 \times 10^{-4}$	$0.0003 \pm 2 \times 10^{-4}$
honeycomb	$0.00013 \pm 6 \times 10^{-5}$	$0.0006 \pm 3 \times 10^{-4}$	$0.0004 \pm 6 \times 10^{-4}$	$0.0007 \pm 6 \times 10^{-4}$	$0.0009 \pm 3 \times 10^{-4}$

Table 6.5: Max friciton coeff

nocut	$0.0139 \pm 9 \times 10^{-4}$	$0.0083 \pm 7 \times 10^{-4}$	$0.010 \pm 1 \times 10^{-3}$	$0.0105 \pm 9 \times 10^{-4}$	
popup	$0.007 \pm 2 \times 10^{-3}$	$0.010 \pm 2 \times 10^{-3}$	$0.007 \pm 2 \times 10^{-3}$	$0.009 \pm 3 \times 10^{-3}$	$0.006 \pm 2 \times 10^{-3}$
honeycomb	$0.010 \pm 1 \times 10^{-3}$	$0.007 \pm 2 \times 10^{-3}$	$0.007 \pm 3 \times 10^{-3}$	$0.000 \pm 3 \times 10^{-3}$	$0.004 \pm 3 \times 10^{-3}$

One theory for the low friction coefficient might depend on the fact that the normal force is only applied on the pull blocks. Especially with the cut sheet the tension drops such that the effective normal force on the inner sheet is not changing very much. By this theory the friction force vs. normal force on the pull blocks should look a bit more like expected and we might make some plots of those to check

When looking at the graphs for the PB the max friction is visually textbook linear, while the mean friction is a bit more linear but also with negative coefficients...

6.7 Computational cost

Talk about the computational cost of different choices. How does computation time scale with drag speed, dt and maybe T and K as well. One could also mention scaling with system size.

Show how the number of cores per simulation scale to argue that running on just one core (maybe 4) is smart for the next step of many simulations.

Mention the trouble with GPU to show that this was considered, and in fact this was the reason for choosing the Tersoff potential over the AIREBO which is perhaps more common these days...

Chapter 7

Generating data

Present the configuration and variable choices for the generated dataset. Perhaps include appendix with all the configurations shown in a grid

Chapter 8

Training forward network

Chapter 9

Inverse design

Chapter 10

Negative friction coefficient

10.1 Simulated coupling of normal force and stretch

10.2 Nanomachine coupling

Attempt to couple normal force and stretch by crossed carbon nanotube (CNT) contraption 10.1.

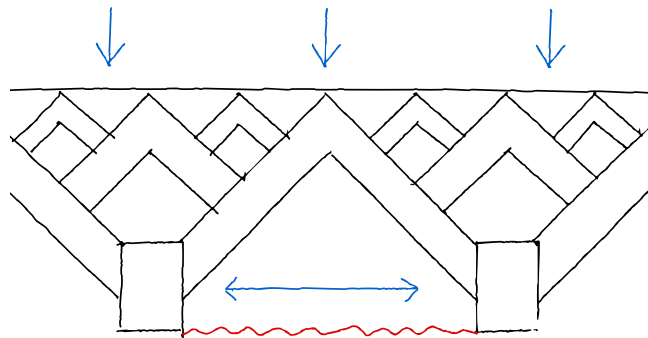


Figure 10.1: Working sketch for nanomachine

Summary

10.3 Summary and conclusion

10.4 Outlook / Perspective

- What did we not cover?
- What kind of further investigations does this study invite?

Things to include here

- Could be valuable to spend more time on the validation of the MD simulations. How does material choice and potential effects the results. How realistic is the simulations?
- Are there any interesting approaches for compressed kirigami structures?
- How does these results scale? I imagined that the nanomachine systems should be applied in small units to avoid scaling problems, but in general I could spend way more time on the scaling investigation.
- Since the normal force is applied at the pull blocks the normal force distribution changes from the sides more towards and even distribution as the sheet is put under tension (stretched). If we imagined a sheet for which the center part was either a different material or had some kind of pre-placed asperity on it, could we then exploit this force distribution to get exotic properties as well? By studying this we might get a clearer understanding of what is the cause of my results.

Appendices

Appendix A

Bibliography

- [1] E. Gnecco and E. Meyer, *Elements of Friction Theory and Nanotribology*. Cambridge University Press, 2015, 10.1017/CBO9780511795039.
- [2] Bhushan, *Introduction*, ch. 1, pp. 1–? John Wiley & Sons, Ltd, 2013.
<https://onlinelibrary.wiley.com/doi/pdf/10.1002/9781118403259.ch1>.
<https://doi.org/10.1002/9781118403259.ch1>.
- [3] H.-J. Kim and D.-E. Kim, *Nano-scale friction: A review*, .
- [4] K. Holmberg and A. Erdemir, *Influence of tribology on global energy consumption, costs and emissions*, .
- [5] J. Norell, A. Fasolino and A. Wijn, *Emergent friction in two-dimensional frenkel-kontorova models*, *Physical Review E* **94** (04, 2016) .
- [6] P. Z. Hanakata, E. D. Cubuk, D. K. Campbell and H. S. Park, *Forward and inverse design of kirigami via supervised autoencoder*, *Phys. Rev. Res.* **2** (Oct, 2020) 042006.
- [7] P. Z. Hanakata, E. D. Cubuk, D. K. Campbell and H. S. Park, *Accelerated search and design of stretchable graphene kirigami using machine learning*, *Phys. Rev. Lett.* **121** (Dec, 2018) 255304.
- [8] R. W. Liederink, B. Weber, C. Coulais and D. Bonn, *Geometric control of sliding friction*, *Extreme Mechanics Letters* **49** (2021) 101475.
- [9] N. Manini, O. M. Braun, E. Tosatti, R. Guerra and A. Vanossi, *Friction and nonlinear dynamics*, *Journal of Physics: Condensed Matter* **28** (jun, 2016) 293001.
- [10] B. Bhushan and A. V. Kulkarni, *Effect of normal load on microscale friction measurements*, *Thin Solid Films* **278** (1996) 49–56.
- [11] J. Gao, W. D. Luedtke, D. Gourdon, M. Ruths, J. N. Israelachvili and U. Landman, *Frictional forces and amontons' law: From the molecular to the macroscopic scale*, .
- [12] Y. Mo, K. T. Turner and I. Szlufarska, *Friction laws at the nanoscale*, .
- [13] G. Carbone and F. Bottiglione, *Asperity contact theories: Do they predict linearity between contact area and load?*, *Journal of the Mechanics and Physics of Solids* **56** (2008) 2555–2572.
- [14] W. Commons, *File:asperities.svg — wikimedia commons, the free media repository*, 2022.
- [15] J. A. Greenwood and J. B. P. Williamson, *Contact of nominally flat surfaces*, Dec, 1966. 10.1098/rspa.1966.0242.
- [16] B. N. J. Persson, *Theory of rubber friction and contact mechanics*, *The Journal of Chemical Physics* **115** (2001) 3840–3861, [<https://doi.org/10.1063/1.1388626>].
- [17] B. Luan and M. O. Robbins, *The breakdown of continuum models for mechanical contacts*, .
- [18] M. Dienwiebel, N. Pradeep, G. S. Verhoeven, H. W. Zandbergen and J. W. Frenken, *Model experiments of superlubricity of graphite*, *Surface Science* **576** (2005) 197–211.
- [19] J. A. van den Ende, A. S. de Wijn and A. Fasolino, *The effect of temperature and velocity on superlubricity*, *Journal of Physics: Condensed Matter* **24** (oct, 2012) 445009.
- [20] X. Zhao, M. Hamilton, W. G. Sawyer and S. S. Perry, *Thermally activated friction*, .
- [21] S. Y. Krylov, K. B. Jinesh, H. Valk, M. Dienwiebel and J. W. M. Frenken, *Thermally induced suppression of friction at the atomic scale*, *Phys. Rev. E* **71** (Jun, 2005) 065101.
- [22] B. Bhushan, *Nanotribology and nanomechanics*, *Wear* **259** (2005) 1–?
- [23] P. Zhu and R. Li, *Study of nanoscale friction behaviors of graphene on gold substrates using molecular dynamics*, .

- [24] J. Zhang, E. Osloub, F. Siddiqui, W. Zhang, T. Ragab and C. Basaran, *Anisotropy of graphene nanoflake diamond interface frictional properties*, *Materials* **12** (2019) .
- [25] F. Bonelli, N. Manini, E. Cadelano and L. Colombo, *Atomistic simulations of the sliding friction of graphene flakes*, .
- [26] X. Feng, S. Kwon, J. Y. Park and M. Salmeron, *Superlubric sliding of graphene nanoflakes on graphene*, .
- [27] M. Reguzzoni and M. C. Righi, *Size dependence of static friction between solid clusters and substrates*, *Phys. Rev. B* **85** (May, 2012) 201412.
- [28] J. H. Dieterich, *Time-dependent friction in rocks*, *Journal of Geophysical Research (1896-1977)* **77** (1972) 3690–3697, [<https://agupubs.onlinelibrary.wiley.com/doi/pdf/10.1029/JB077i020p03690>].
- [29] U. D. Schwarz, O. Zwörner, P. Köster and R. Wiesendanger, *Quantitative analysis of the frictional properties of solid materials at low loads. i. carbon compounds*, *Phys. Rev. B* **56** (Sep, 1997) 6987–6996.
- [30] S. Li, Q. Li, R. W. Carpick, P. Gumbsch, X. Z. Liu, X. Ding et al., *The evolving quality of frictional contact with graphene*, .
- [31] J. Tersoff, *New empirical approach for the structure and energy of covalent systems*, *Phys. Rev. B* **37** (Apr, 1988) 6991–7000.
- [32] Q. Zhang, D. Diao and M. Kubo, *Nanoscratching of multi-layer graphene by molecular dynamics simulations*, *Tribology International* **88** (2015) 85–88.
- [33] H. M. Yoon, Y. Jung, S. C. Jun, S. Kondaraju and J. S. Lee, *Molecular dynamics simulations of nanoscale and sub-nanoscale friction behavior between graphene and a silicon tip: analysis of tip apex motion.*, *Nanoscale* **7** **14** (2015) 6295–303.
- [34] S. Corporation, “pair_style lj/cut command.”
- [35] X. Wang, S. Ramírez-Hinestrosa, J. Dobnikar and D. Frenkel, *The lennard-jones potential: when (not) to use it*, *Phys. Chem. Chem. Phys.* **22** (2020) 10624–10633.
- [36] R. Naeem, “Lennard-jones potential.”
- [37] S. Corporation, “pair_style sw command.”
- [38] F. H. Stillinger and T. A. Weber, *Computer simulation of local order in condensed phases of silicon*, *Phys. Rev. B* **31** (Apr, 1985) 5262–5271.
- [39] S. Corporation, “pair_style tersoff command.”
- [40] T. Schneider and E. Stoll, *Molecular-dynamics study of a three-dimensional one-component model for distortive phase transitions*, *Phys. Rev. B* **17** (Feb, 1978) 1302–1322.